Utrecht University

QuTech

UTRECHT UNIVERSITY

MASTERS THESIS

Investigating Quasiparticle Poisoning in Floating Hybrid Double Dot Devices Using Gate-Based Sensing

---

Author:
Nejc BLAZNIK
(5713625)

Supervisors:
Prof. Dr. Peter van der Straten
Prof. Dr. Ir. Leo. P Kouwenhoven
MSc. Damaz de Jong
MSc. Christian Prosko

A thesis submitted in fulfillment of the requirements
for the degree of Master of Science

August 15, 2020

UTRECHT UNIVERSITY

Abstract

Faculty of Science
Department of Physics

Master of Science

Investigating Quasiparticle Poisoning in Floating Hybrid Double Dot Devices Using Gate-Based Sensing

by Nejc BLAZNIK

One of the essential limitations for a physical realisation of topological-qubit based quantum computing, is the problem of uncontrolled quasiparticle poisoning of the superconducting charge island. These quasiparticles have been previously reported as a known limiting factor in most of the superconducting architectures. To this end, we consider the importance of equilibrium quasiparticle poisoning in hybrid semiconducting-superconducting systems believed to be able to host Majoranas.

We employed gate-based dispersive sensing by investigating a reflected radio-frequency (RF) signal from a resonator, which is capacitevly coupled to one of the gate electrodes of the hybrid double dot realised in an InAs nanowire. This way, the quantum capacitance of the system can be probed, which in turn reveals charge-tunnelling processes, and can be used as an indicator of single-electron tunnelling events. By operating the device in a so-called floating regime, where a double dot system is entirely decoupled from the leads, external non-equilibrium quasiparticle poisoning events can be exponentially suppressed. By appropriately tuning the chemical potentials on the quantum dot and the superconducting island, we attempt to scrutinise the dynamics of the quasiparticles innate to the superconductor. We investigated the dependence of quasiparticle tunnelling rates on the temperature of the system, as well as the applied RF power, as both are predicted to increase the average number of quasiparticles on the island. In both cases, we could find no observational proof of quasiparticle tunnelling events through the use of our measurement technique. We report an observation of a two-level resonator response, which we explain using a two-level fluctuator. Analysing telegraph measurements, we demonstrate the viability of the analysis tool, which allows us to determine average occupation times of each state. In principle, for processes occurring at rates slower than the measurement frequency, this technique can be used to convert a relatively faint difference between the “poisoned and unpoisoned state”, to the signal of the gate being on coulomb resonance versus on coulomb blockade, which is a much clearer signal to distinguish. Both, the technique as well as the expected rates of the physical processes within the island are evaluated in the context of the experiment.

Contents

List of Abbreviations and Symbols

TQC	**T**opological **Q**uantum **C**omputing
MZM	**M**ajorana **Z**ero **M**ode
MBS	**M**ajorana **B**ound **S**tate
TS	**T**opological **S**uperconductivity
QPs	**Q**uasi**p**articles
CSD	**C**harge **S**tability **D**iagram
QPP	**Q**uasi**p**article **P**oisoning
DOS	**D**ensity **O**f **S**tates
IQ Space	**I**n-phase and **Q**uadrature Space
SNR	**S**ignal-to-**N**oise **R**atio
NW	**N**ano**w**ire
RF	**R**adio **F**requency

L	Resonator Inductance
C_p	Parametric Capacitance
C_q	Quantum Capacitance
C_t	Tunnelling capacitance
E_c^{QD}	Charging Energy of the Quantum Dot
E_c^{SC}	Charging Energy of the Superconducting Island
$\widetilde{\Delta}$	The Energy of the Lowest Single-Particle State (on SC)

Chapter 1

Introduction

QUANTUM COMPUTING is a recent but very promising area of research, which intertwines two of the most significant advancements in science and technology of the last century - computing and quantum mechanics. A quantum computer relying on the fundamental phenomena of quantum mechanics such as *superposition* and *entanglement* could solve some classical problems orders of magnitude faster than any classical computer resulting in faster search and prime factorisation [1, 2] algorithms, as well as provide secure communications channels [3], and simulate quantum systems [4]. The latter is one of the most promising and potentially impactful applications of quantum computing. Such simulations could be used to simulate the dynamics of complex chemical reactions, with potentially revolutionary applications in the fields of pharmacology, material sciences, energy storage and computational chemistry, to name a few. (For a review see, e.g. ref. [5, 6].)

The fundamental building block of a quantum computer is a quantum bit or a *qubit*, which can be represented by any two-level quantum mechanical system. The central and defining difference is that a qubit can be in a coherent superposition between two orthonormal states, $|0\rangle$ and $|1\rangle$ (e.g. spin-up and spin-down of an electron), as opposed to a classical bit which can take *either* one of the two values, 1 or 0. A qubit can be realised in a variety of physical systems, with currently the most focus dedicated towards superconducting circuits, spinful quantum dots, NV centres in diamond and trapped ions [7, 8]. However, a significant difficulty for nearly all of the qubit architectures seems to arise from two seemingly contradictory requirements. On the one hand, qubits are extremely sensitive to destructive environmental noise, so to ensure long coherence times, the microscopically small quantum system should be nearly entirely isolated. On the other hand, to perform measurements and ensure that the system evolves in the desired manner, the processing unit itself cannot be perfectly isolated. To battle decoherence, quantum error correction can be employed, resulting, however, in a much larger number of required qubits [9]. Another radically different approach towards circumventing the decoherence problem is topological quantum computing (TQC).

A topological qubit[1] is based on exotic quasiparticle excitations called *non-Abelian*

---

[1] The focus of this thesis is not primarily on topological quantum computing, but an overview of the field can be found in [10]

anyons. The main appeal of such qubit comes from its topological protection from the environmental noise, where the qubit state information is encoded in multiple spatially separated anyons. Moving one anyon around another, or *braiding*, can completely change the state of a system within the degenerate ground-state manifold. This property can be used to define stable logic gates needed for quantum computation [11], where rather than physically moving two particles, recent efforts have focused on effective *measurement-based braiding*, which can be achieved by measuring the joint occupational parity of a pair of particles [12–14]. Recently, one of the most investigated candidates of non-Abelian anyons are so-called Majorana zero-energy modes (MZMs)[2] [15], which are predicted to arise as boundary states of some systems once they enter a spinless p-wave topological superconducting (TS) phase [16].

Although the leading appeal behind Majorana-based quantum computers is the topological protection from decoherence, Majorana qubit dephasing can still occur via incoherent exchange of parity due to insufficient separation of the two MZMs [17] or via uncontrolled relaxation of single-electron-like excitations known as quasiparticles[3] (QPs) into the Majorana subspace, also called quasiparticle poisoning (QPP) of the Majorana qubit [18]. Quasiparticles are present in any realistic physical superconductor, and their effects have been explored in the context of superconducting [19–22] as well as semiconductor-superconductor hybrid devices [23–25]. The latter, in particular, are more susceptible to poisoning as the induced superconducting gap is reduced, and subgap states might appear.

Quasiparticles may originate from different mechanisms; they can be created within the island by an external (even cosmogenic) environmental radiation, they can be thermally excited within the Majorana qubit system, or they might be located in one of the non-topological subgap states. While the external non-equilibrium quasiparticle poisoning can be suppressed for a system decoupled from the leads [26], experiments show that at low temperatures quasiparticle concentrations in the system are not exponentially suppressed, as suggested by theory [27]. Instead, QP density saturates to a constant value [19, 21], as the rate of QP recombination into Cooper pairs becomes exponentially slow for decreasing densities of the QPs [28]. Although much experimental work has been dedicated to protection from quasiparticle poisoning, it remains a critical limiting factor. It is estimated that in the presence of quasiparticles, the Majorana-based qubit lifetime ranges between 10 ns to 0.1 ms [23], which might be problematically low for some qubit gate implementations.

To investigate QPP rates, we attempt to measure single-quasiparticle tunnelling events from a superconducting island by employing gate-based resonator sensing.

---

[2] Also known as Majorana bound states (MBSs)

[3] Commonly the term "quasiparticle" is used to describe a variety of emerging phenomena. For most cases in the thesis, Majorana quasiparticles will be referred to as "Majoranas" or "Majorana zero modes", while the trapping of excess unpaired electrons on the superconductor as "quasiparticle poisoning".

Using reflectometry[4] we monitor *changes* in the average charge of a device by scrutinising its quantum capacitance, $\partial\langle Q\rangle/\partial V_g$, using an LC resonator capacitively coupled to one of the existing gate electrodes defining the double dot [14]. In a dispersive limit[5] this measurement technique enables high-fidelity readout for both superconducting [29] and Majorana qubits [14]. It allows for the measurement of an electron tunnelling rate, which is an indicator of the state of the system - different qubit states will impart different dispersive shifts on a resonator. This readout technique offers several advantages such as reducing the number of on-chip components as well as the ability to probe the system locally within the Coulomb blockaded region.

Although relatively well explored, the investigation of quasiparticle poisoning was mostly performed in systems kept in contact with the leads, which are in itself a big source of quasiparticles [26]. With recent advances in the dispersive readout, the requirement for the leads is alleviated, with some proposals for Majorana qubit architectures allowing the systems to be operated and probed without any need for the leads [13, 14]. Thus we feel motivated to further explore quasiparticle poisoning processes happening within the island itself. The experiment described in this thesis is the first time *time-resolved* quasiparticle poisoning is investigated in a superconductor-semiconductor hybrid system that is completely decoupled from the leads. It allows for all detected quasiparticle poisoning events to be associated with the processes related to the SC itself.

1.1 Outline

The goal of this thesis is to introduce the theory of mesoscopic systems composing of a charge island and a quantum dot, elucidate the working principles of gate-based resonator sensing and use it to perform time-resolved measurements of quasiparticle dynamics on the SC island. In Chapter 2, the theoretical background of quantum dot theory, superconductivity and gate-based reflectometry sensing is introduced. In Chapter 3, the experimental setup is outlined, starting from the large scale refrigerators down to the smallest units of few μm in scale, the double dot device. Chapter 4 contains the core of the experiment, where we investigate quasiparticle dynamics by intentionally inducing poisoning events, either by increasing the power of the readout signal or by increasing the temperature of the device. Additionally, we attempt to provide the reasoning for the observations. The main results are summarised in the final Chapter 5, where we once again review the experiment and its possible improvements and extensions in the future.

---

[4] As we will explain later in the thesis, experimentally we are interested in the reflection coefficient of the resonator (S_{11}), which is measured indirectly via the transmission coefficient (S_{21}) of the feedline circuit.

[5] Regime where the detuning between the resonator and qubit transition frequency is much larger than the interaction strength

Chapter 2

Theoretical Background

This chapter presents the theoretical background behind some of the key concepts used in the thesis. First, an overview of charge islands and quantum dots is offered, followed by a crash-course in superconductivity. Lastly, a theoretical model behind gate-based sensing is presented.

2.1 Quantum Dots

Treatment of the systems dealt with in this thesis starts with charging physics of artificially fabricated sub-micron structures in semiconductors, allowing for investigation of electron transport features. In such structures, electrostatic interaction between electrons can give rise to essential phenomena called Coulomb blockade, which can be utilised to construct single and double quantum dots (QD and DQD, respectively) - the central structures investigated in this thesis.

2.1.1 Electron Tunnelling

Consider several electrons, N, on an isolated conductor small enough, so that the energy cost needed to add another charge is significant due to the electrostatic repulsion between the electrons at the Fermi level. Such a conductor then acts as a *charge island* for electrons. The charge on such islands is quantised and equals to Ne, and if electrons are allowed to tunnel to and from the island, the total charge changes by a multiple of the elementary charge e. Conveniently, the change of the Coulomb energy due to tunnelling can be expressed in terms of the capacitance C of the island. If an extra charge e is added to the system, the electrochemical potential changes by the *charging energy* $E_C = e^2/C$. In order to resolve single-electron tunnelling events, two main conditions must be met due to the discrete nature of charges; firstly, the island must be coupled to a terminal, but not too strongly. This connection is called a tunnel junction, and by relating typical timescales on which tunnelling events occur with the Heisenberg's uncertainty relation, the limit for its resistance can be established. Secondly, the energy due to thermal fluctuations should be much smaller

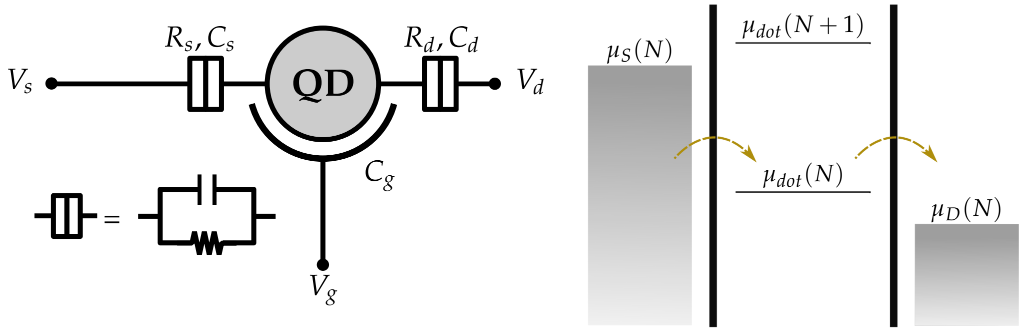

(a) (b)

FIGURE 2.1: **(a)** A schematic depiction of a single quantum dot coupled via tunnel barriers to the source and drain terminals. By applying voltage on the source, drain and gate voltage V_s, V_d, V_g, chemical potentials of source, drain and the quantum dot can be tuned, allowing for the tunnelling to occur, or be suppressed. **(b)** A density of states energy representation of the system in part (a). The difference in chemical potentials of the source and drain leads defines a bias window. If states of quantum dot are available within such window, the current is non-zero. Arrows represent the path of electrons tunnelling.

than the charging energy. The two conditions can be summarised as [30]

$$R \ll h/e^2 \approx 12.9\ k\Omega \tag{2.1a}$$

$$e^2/C \gg k_B T \tag{2.1b}$$

The first condition is met by weakly coupling the island to the source and drain terminals and the second one by reducing the total capacitance of the charge island (for example by moving the gates further from the island) and lowering the temperature. The devices presented in this thesis have charging energies on the order of few 100 μeV, implying cryogenic sub-kelvin working temperatures to prevent thermal excitations.

2.1.2 Single Quantum Dot

If the charging island is small enough, and the orbital electronic energy spacing becomes significant, a *quantum dot* is formed. Quantum dots allow for circuit-based investigation of quantum mechanical phenomena, through single-electron transport on and off the island. The most straightforward implementation of a quantum dot is a single dot coupled to the source and drain contacts, as well as a third gate, used to adjust the amount of charge on the island. A schematic representation of such a device is given in Fig 2.1a.

To calculate the total energy of the system with N electrons on the island and source, drain and gate terminal voltages V_s, V_d, V_g respectively, one can make use of a constant interaction model, where all capacitances are assumed to be fixed[1] [30, 31]. The resulting (ground state) energy is then given by [32]

---

[1] This assumption is justified if the size of a quantum dot is much larger than the average screening length, i.e. there are no electric fields inside the dot.

$$U(N) = \frac{[-(N-N_0)|e| + C_s V_s + C_g V_g + C_d V_d]^2}{2C} + \sum_{p=1}^{N} E_p, \tag{2.2}$$

with N_0 the number of electrons intrinsically present on the island without any voltage applied to either of the electrodes, and $C = C_s + C_g + C_d$, the total capacitance of the island[2]. The first part of the equation above is the purely classical electrostatic contribution of a capacitor, whereas the second term includes the ground energy of the p electrons in the dot at zero temperature, resulting from the quantum mechanical confinement, as the sum over the single particle energies E_p. As mentioned earlier, this extra energy is the reason we refer to the charge island as a quantum dot. A more interesting quantity in electron transport however, is the electrochemical potential $\mu(N)$ of the states in the dot, defined as the minimum energy cost for adding the N-th electron to the dot

$$\begin{aligned}\mu(N) \equiv & U(N) - U(N-1) \\ = & E_N + E_C(N - N_0 - 1/2) - \frac{e}{C}(C_s V_s + C_g V_g + C_d V_d),\end{aligned} \tag{2.3}$$

with an E_N the ground state orbital energy of the Nth electron state[3]. The spacing of discrete energy levels in the quantum dot can be defined as the addition energy of a quantum dot

$$E_{add}(N) = \mu(N+1) - \mu(N) = E_C + \Delta E_N, \tag{2.4}$$

with $\Delta E_N = E_{N+1} - E_N \ll E_C$ the energy spacing between two subsequent orbitals[4].

By varying the gate voltage V_g, the number of electrons on the dot can be changed. The system can be visualised in the density of states (DOS) representation, as in Fig 2.1b. By applying a finite bias source-drain voltage $V_{sd} = V_s - V_d = (\mu_s - \mu_d)/e$, a transport window between the chemical potentials of the Fermi levels of source and drain can be defined. If the number of available states on the dot in such energy window is non-zero, then electrons can tunnel through, and therefore a non-zero current is

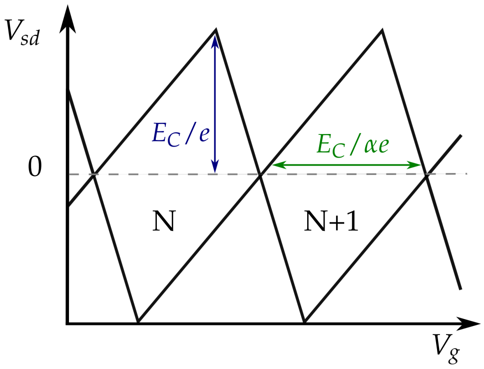

FIGURE 2.2: Coulomb Diamonds

---

[2] Notice that for a single electron ($N - N_0 = 1$, and $C_s V_s + C_g V_g + C_d V_d = 0$), equation 2.2 yields charging energy $E_C = e^2/2C$. For the description presented here, it is, however, more convenient to take $E_C = e^2/C$ as the unit of charging energy.

[3] This equation can be understood in a more familiar form as the sum of the chemical potential $\mu_{ch}(N) = E_N$ resulting from quantum effects and the electrostatic potential resulting form the 'classical' part relating to capacitances.

[4] In many-electron regime, the difference in the energy of two subsequent orbitals, $E_{N+1} - E_N$, usually decreases with addition of more electrons. For the case of systems investigated in this thesis, this number is on the order of $10 - 100\mu eV$.

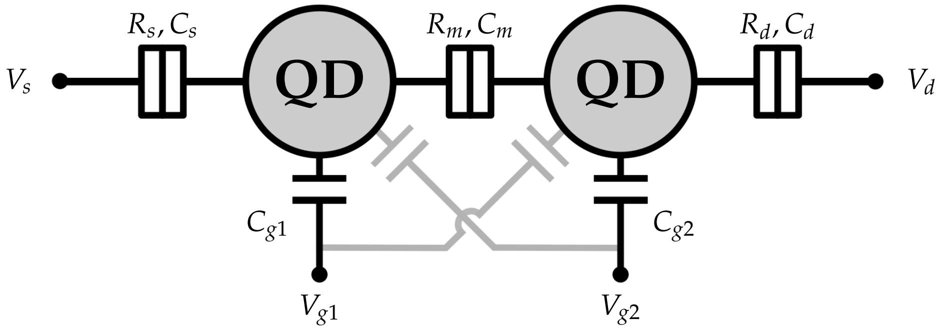

FIGURE 2.3: Double Quantum Dot. In real systems potential cross-capacitances between dot 1(2) and plunger gate $V_{g2(1)}$, shown in light grey.

observed. However, if no states are available within the window, the current cannot flow, and the system is said to be in *Coulomb blockade*. This relation between the current, and the voltages applied to the system, can be conveniently expressed in a *Coulomb diamonds* scan (Fig. 2.2), where the diamond-shaped regions denote voltage configurations where no current can run. From the dimensions of these diamonds, several useful quantities can be calculated, such as all capacitances and the charging energy of the quantum dot, as well as the *gate lever arm* $\alpha = C_g/C < 1$ of the system; a measure of how well the applied gate voltage is converted into chemical potential induced on the dot.

In the rest of this thesis, theory and experiments will be restricted to the *linear response regime*, where the bias voltage is ~ 0. This simplifies the Eq. 2.3 to

$$\mu(N) = E_C(n - 1/2) - e\alpha V_g + E_N, \tag{2.5}$$

with $n = (N - N_0)$ the excess number of charges on the dot.

2.1.3 Double Quantum Dot

The extension to a double dot is relatively straightforward - a second quantum dot can be added in series with the first one. As single quantum dots are often called "artificial atoms" due to their discrete energy spectrum, two or more quantum dots can form an "artificial molecule", with some inter-dot coupling. A circuit describing a double quantum dot is depicted in Fig. 2.3. If the electrons are localised on individual dots, static redistribution of charge leads to attractive Coulomb interaction, resulting in a weak binding, analogous to that of ionic bonding. If instead two-electron states are quantum-mechanically coupled, and the electron can freely tunnel in a phase-coherent way between two degenerate energy levels in the two dots, a covalent-like bond occurs. In such case, the electron can no longer be regarded as a particle residing on one of the dots, but must rather be considered as a coherent wave delocalised over the two dots.

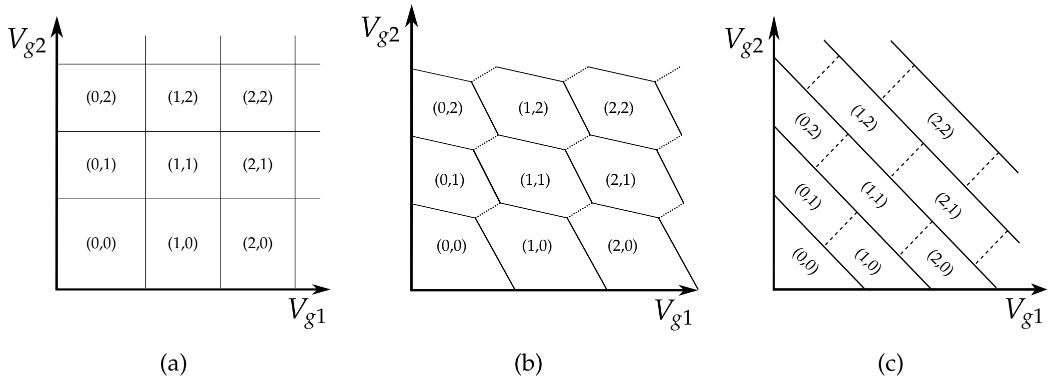

(a) (b) (c)

FIGURE 2.4: A charge stability diagram for a double quantum dot. Part a) is for zero inter-dot coupling, b) for intermediate, and c) for strong.

The extension of the model presented in 2.1.2 is trivial. Analogous to the case for a single dot, each dot is defined by tunnelling barriers and is capacitively coupled to gate voltage $V_{g1(2)}$ through a capacitor $C_{g1(2)}$. The two dots are also coupled to each other through a tunnel barrier represented by a capacitor C_m and a resistor R_m connected in parallel. Assuming linear transport regime with negligible cross-capacitances (e.g. between dot 1 and V_{g2}) and any other stray fields, the total electrostatic energy as a function of charges on the island can be written as [33]

$$\begin{aligned} U(N_1,N_2) =& \frac{1}{2}N_1^2E_{C1}+\frac{1}{2}N_2^2E_{C2}+N_1N_2E_{Cm}+f(V_{g1},V_{g2}) \\ f(V_{g1},V_{g2}) =& \frac{1}{-|e|}\Big[C_{g1}V_{g1}(N_1E_{Cm}+N_2E_{Cm})+C_{g2}V_{g2}(N_1E_{Cm}+N_2E_{Cm})\Big] \\ &+\frac{1}{e^2}\Big[\frac{1}{2}C_{g1}^2V_{g1}^2E_{C1}+\frac{1}{2}C_{g2}^2V_{g2}^2E_{C2}+C_{g1}V_{g1}C_{g2}V_{g2}E_{Cm}\Big] \end{aligned} \tag{2.6}$$

where $E_{C1(2)}$ denotes the charging energy of dot 1(2) and E_{Cm} is the electrostatic coupling energy, describing the change in energy of a dot, when an electron is added to the other dot. In terms of capacitances, these can be expressed as

$$E_{C1} = \frac{e^2}{C_1}(1-C_m^2/C_1C_2)^{-1} \tag{2.7a}$$

$$E_{C2} = \frac{e^2}{C_2}(1-C_m^2/C_1C_2)^{-1} \tag{2.7b}$$

$$E_{Cm} = \frac{e^2}{C_m}(C_1C_2/C_m^2-1)^{-1} \tag{2.7c}$$

where $C_{1(2)}$ denotes the sum of all capacitances attached to the dot 1(2). These can be seen as charging energies of a single quantum dot corrected with a factor accounting for capacitive coupling. A full derivation, analogous to the one presented in 2.1.2, together with reduced forms of Eq. 2.6 for cases of weak and strong inter-dot capacitances, as well as the derivations of electrochemical potentials for each dot, are provided in [33].

Similar to the Coulomb diamonds, we can represent regions of Coulomb blockade in a *charge stability diagram* (CSD), as in Fig. 2.4. For two quantum dots, this yields a plot of regions of stable charge configuration, with equilibrium electron numbers of the system (N_1, N_2), as a function of the two gate voltages V_{g1} and V_{g2}. Charge stability diagrams for three different regimes of inter-dot coupling are shown. For $C_m = 0$, i.e. completely decoupled dots, the change in gate voltage $V_{g1(2)}$ will affect solely the charge on dot 1(2) 2.4a. In the intermediate regime, the grid becomes hexagonal (Fig. 2.4b), with the vertices of the domains being dubbed the "triple-points". In the limit $C_m/C_{1(2)} \rightarrow 1$, the triple-point separation is at maximum, and the system can be modelled as an effective single dot system with $(N_1 + N_2)$ charges, and a capacitance of $C_1 + C_2 - 2C_m$.

As before, a multitude of information can be inferred experimentally from such plots. Solid lines connecting two triple-points, separating different charge states, can be understood as tuning configurations allowing for the electron to be delocalised between the two dots when two energy levels are aligned, or *degenerate* (see Fig. 2.5). From the parameters indicated in the figure, in combination with the gate lever arm (obtained from the individual diamond scans of each dot), all capacitances can be determined.

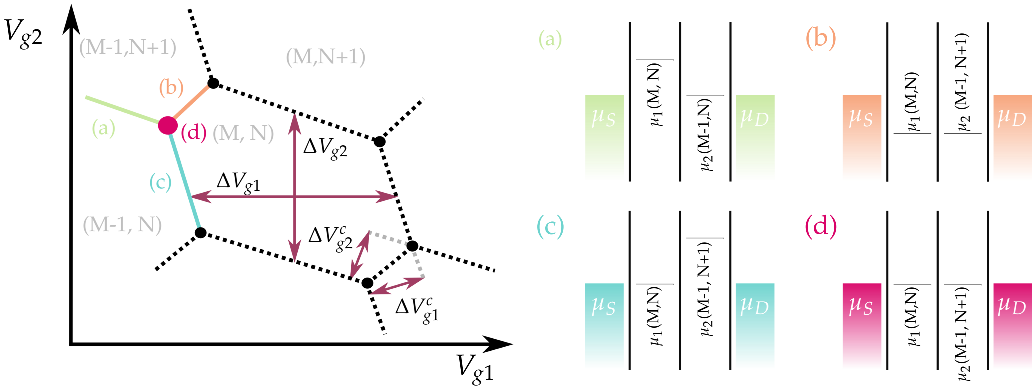

FIGURE 2.5: Zoomed in diagram of the a single hexagon in a CSD for intermediate tunnel coupling, at zero bias. From the parameters indicated, together with the gate lever arm, all capacitances can be calculated. In the diagram, different lines representing different configurations allowing for the tunnelling of charges, where different conditions are met; either the source chemical potential is aligned with the chemical potential of the first dot (blue line), the chemical potential of the second dot is aligned with the drain chemical potential (green line), or the chemical potentials of the two dots are aligned, allowing for the inter-dot tunnelling. At the so-called triple points (red dot), all three of these conditions are met simultaneously. In the diagram, the dimensions of the hexagon can be used to determine characteristic charging energies as well as the capacitances of the system; $\Delta V_{g1} = E_{C1}/e\alpha_1$, $\Delta V_{g2} = E_{C2}/e\alpha_2$, $\Delta V^c_{g1} = E_{C1}C_m/C_2e\alpha_1$ and $\Delta V^c_{g2} = E_{C2}C_m/C_1e\alpha_2$.

2.2 Superconductivity

One of the key ingredients necessary for the realisation of Majorana bound states is induced superconductivity. As the temperature is decreased below a particular critical temperature T_C, many materials enter a superconducting phase, characterised by the zero resistance to an electric current [34], as well as the expulsion of magnetic fields from the bulk of superconductor [35]. This extraordinary feature of nature allows for direct observation of quantum mechanical phenomena macroscopically and is, therefore, an ideal platform for realising a quantum computing system. Even though the first experimental observation of superconductivity was already provided in 1911 by Heike Kamerlingh Onnes, it took nearly fifty years before the first microscopic theory of superconductivity was proposed by J. Bardeen, L. N. Cooper and J. R. Schrieffer (BCS Theory) [36]. Since then, superconducting materials have been a subject of scrutinising scientific research and were most notably implemented as extremely high power (MRI/NMR machines, particle accelerators, plasma confining tokamak magnets) and extremely sensitive electromagnets (various magnetometers based on superconducting quantum interference devices (SQUIDs) using Josephson junctions).

2.2.1 BCS Theory

The BCS theory stands at the centre of this thesis. It describes superconductivity as a microscopic effect arising as a consequence of electrons constructively interacting with positive atoms in the crystal lattice of the material, which in turn attracts another electron with opposite spin. Through such electron-phonon interaction, the effective attractive potential between the two electrons of opposite momentum and spin will cause them to become correlated. A pair of such electrons is known as a Cooper pair, and as long as the thermal energy attempting to break them apart is small enough, the pair will stay together. A Cooper pair can now be seen as a composite boson. At sufficiently low temperatures all Cooper pairs can occupy the lowest zero-momentum energy state, thus undergoing Bose-Einstein condensation and forming a charged superfluid liquid condensate. This roughly explains why superconductivity requires low temperatures.

An obvious, and interesting problem arises with the quantum transport on the interface between a normal conductor, and a superconductor. According to the BCS description of the current, a single electron seemingly cannot induce a current through the SC. Yet, it does. This occurs through a process called *Andreev reflections*. This scattering process describes how the normal current can be converted into supercurrent. When an electron from the normal state material at energies too low to enter the superconductor is incident on the interface with a superconducting material, the electron will form a Cooper pair in the SC, *and* a retro-reflected hole of opposite velocity and spin but equal momentum, in the normal conductor. Due to time-reversal symmetry, this process comes in alternative flavour as well; where an incident hole is retro-reflected into an electron.

The energy spectrum of a superconductor can better be understood by first considering charge carriers in a normal metal with a Fermi gas model. At zero temperature, the electrons form a momentum space, where all the states up to the Fermi surface are occupied, and all the states above are empty. According to the BCS theory, the charge carriers in the superconductor are pairs of electrons, so it can be considered a *Fermi liquid*, for which (as shown by Landau in 1956) the treatment is not that much different. The superconductor can then be visualised as a Fermi gas composed of quasiparticles. In the mean-field approximation, the ground state of the superconductor with Cooper pairs is therefore given by

$$|\psi_\varphi\rangle = \prod_{\mathbf{k}} (|u_k| + |v_k| e^{i\varphi} c^*_{\mathbf{k},\uparrow} c^*_{\text{-}\mathbf{k}\downarrow}) |0\rangle \,. \tag{2.8}$$

In the equation above, $|0\rangle$ denotes the electron vacuum state[5], $|u_k|$, $|v_k|$ are numerical factors such that $|u_k|^2 + |v_k|^2 = 1$, and $c^*_{\mathbf{k},\uparrow}$ ($c^*_{\text{-}\mathbf{k}\downarrow}$) is a fermionic creation operator responsible for creating an electron with momentum $\vec{k}$ ($-\vec{k}$) with spin up (down). The two terms in the equation imply, that a Cooper pair can be seen as a superposition of the pair ($\vec{k}\uparrow, -\vec{k}\downarrow$) being occupied (with probability $|v_k|^2$) and being unoccupied (with probability $|u_k|^2$).

2.2.2 Bogoliubov Quasiparticles

Formally, the term quasiparticle is given to any emergent phenomenom behaving as a particle. In the context of Fermi gas, the term quasiparticle is usually used for an excitation above a non-interacting Fermi gas or a Fermi liquid (leaving behind another hole quasiparticle). This thesis, however, will mostly deal with a particular type of quasiparticles - Bogoliubov quasiparticles (sometimes simply named *Bogoliubons*). In the most simple picture, a Bogoliubov quasiparticle is half of the Cooper pair. As opposed to the normal metal, where the phases are random, in superconductors with coherent phases, operators such as $c_{-\mathbf{k}\downarrow} c_{\mathbf{k}\uparrow}$ can have a non-zero expectation values $b_{\mathbf{k}} \equiv \langle c_{-\mathbf{k}\downarrow} c_{\mathbf{k}\uparrow} \rangle$. This is also used to define a *gap function* $\Delta_{\mathbf{k}}$

$$\Delta_{\mathbf{k}} = -\sum_{\mathbf{l}} V_{\mathbf{kl}} b_{\mathbf{l}}, \tag{2.9}$$

with $V_{\mathbf{kl}}$ being the attractive potential responsible for the Cooper-pair formation. In the case considered by Bardeen, Cooper and Schrieffer, the origin of this potential is electron-phonon interaction, with $V_{\mathbf{kl}} = V$, being the measure of the electron-phonon coupling. Bogoliubov showed, that by defining a new Fermi operator $\gamma_{\vec{k}}$, using an appropriate canonical transformation [37]

---

[5] All the states in momentum space up to the Fermi level are occupied.

$$\begin{aligned}\gamma^*_{\mathbf{k}0} &= u^*_{\mathbf{k}} c^*_{\mathbf{k}\uparrow} - v^*_{\mathbf{k}} c_{\text{-}\mathbf{k}\downarrow} \\ \gamma^*_{\mathbf{k}1} &= u^*_{\mathbf{k}} c^*_{\text{-}\mathbf{k}\downarrow} + v^*_{\mathbf{k}} c_{\mathbf{k}\uparrow}\end{aligned} \tag{2.10}$$

and by appropriately choosing coefficients u_k and v_k,

$$|v_{\mathbf{k}}|^2 = 1 - |u_{\mathbf{k}}|^2 = \frac{1}{2}\Big(1 - \frac{\epsilon_{\mathbf{k}}}{E_{\mathbf{k}}}\Big), \tag{2.11}$$

the model Hamiltonian for a general superconductor can be written as [27]

$$H = \sum_{\mathbf{k}} (\epsilon_{\mathbf{k}} - E_{\mathbf{k}} + \Delta_{\mathbf{k}} b^*_{\mathbf{k}}) + \sum_{\mathbf{k}} E_{\mathbf{k}} (\gamma^*_{\mathbf{k}0}\gamma_{\mathbf{k}0} + \gamma^*_{\mathbf{k}1}\gamma_{\mathbf{k}1}), \tag{2.12}$$

with $\epsilon_{\mathbf{k}}$ the energy relative to the chemical potential. The first sum is constant, while the second term gives the increase in energy above the ground state. Thus, the $\gamma_{\mathbf{k}}$ describe the elementary quasiparticle excitations of the system. In equations 2.11, 2.12, we defined

$$E_{\mathbf{k}} = (\epsilon^2_{\mathbf{k}} + |\Delta_{\mathbf{k}}|^2)^{1/2}, \tag{2.13}$$

which at the same time represents the energies of these excitations. Clearly, the minimum excitation energy of the system is the *energy gap* $\Delta_{\mathbf{k}}$, as even at the Fermi surface (i.e. $\epsilon_{\mathbf{k}} = 0$), $E_{\mathbf{k}} = |\Delta_{\mathbf{k}}| > 0$.

2.2.3 Superconducting gap

One of the defining features of a superconductor (and a crucial one in proposed architectures for topological quantum computing) is the superconducting gap - a gap to the next excited state above the condensate, usually on the order of few hundreds μeV for typical superconducting islands investigated here. In simple terms, this means that this gap parameter determines the energy cost for breaking a Cooper pair. The probability for a fermionic quasiparticle to be excited in thermal equilibrium can then be modelled using the Fermi distribution function

$$f(E_{\mathbf{k}}) = (e^{\beta E_{\mathbf{k}}} + 1)^{-1} \tag{2.14}$$

where $\beta = 1/kT$. Naively, this function predicts that at $T = 0$, $f(E_{\mathbf{k}})$ goes to zero for all $\mathbf{k}$. This approximation is good to a certain extent, but as the experimental data shows, at low temperatures quasiparticle density saturates to a constant value [19, 21], yielding a finite density of quasiparticles on the island. In such a case, we say that the island is *poisoned*.

Using equations 2.14 in combination with 2.9, a self-consistent temperature dependence of the superconducting gap, $\Delta(T)$, can be established numerically from [27]

$$\frac{1}{N(0)V} = \int_0^{\hbar\omega_c} \frac{\tanh \frac{1}{2}\beta(\epsilon^2 + \Delta^2)^{1/2}}{(\epsilon^2 + \Delta^2)^{1/2}} d\epsilon, \tag{2.15}$$

with V the measure of the electron-phonon coupling (as defined above), and $N(0)$ the Fermi level electronic density of states. Following [27], this can be evaluated in regimes close to the critical temperature and near 0

$$\Delta \implies \begin{cases} kT_c = 1.13\hbar\omega_c e^{-1/N(0)V} & \text{for } T \to T_c \\ \Delta(0) = 2\hbar\omega_c e^{-1/N(0)V} & \text{for } T \to 0 \end{cases} \tag{2.16}$$

where $\hbar\omega_c$ is a cut-off critical energy related to Debye frequency, and is much smaller than the Fermi energy. The ratio of the two limiting cases yields $2\Delta(0) \approx 3.53kT_c$, one of the most celebrated early predictions of the theory [27]. Physically speaking, as long as the number of thermally excited quasiparticles is low, the gap Δ is nearly constant. On the other side, near the critical temperature $T = T_c$, the order parameter $\Delta(T)$ varies with the square root of $T_c - T$ - Something characteristic of all mean-field theories.

2.2.4 Density of states

Another handy quantity that can be derived is the superconducting density of unpaired electron states $N_s(E)$. The derivation can be simplified significantly, by recognising that the quasiparticle excitations described by the fermionic operator $\gamma^*_{\mathbf{k}}$ are in one-to-one correspondence with the standard metal electron creation operator, $c^*_{\mathbf{k}}$, unaffected by any phase transition. As we are mostly interested in energies in the vicinity of the Fermi energy, the $N(0)$ can be taken to be constant, which leads to a simple result

$$\frac{N(E)}{N(0)} = \begin{cases} \frac{E}{(E^2-\Delta^2)^{1/2}} & (E > \Delta) \\ 0 & (E < \Delta). \end{cases} \tag{2.17}$$

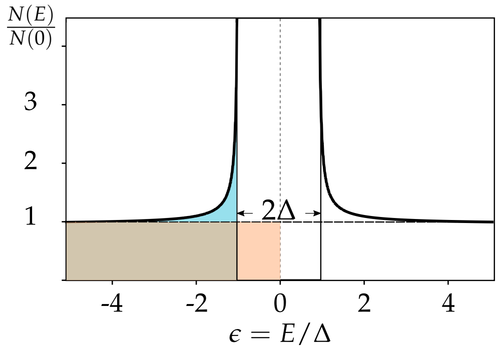

FIGURE 2.6: Density of states in a superconductor. Represented as a function of detuning, in units of Δ ,where states up to the fermi level are already filled. Orange colour represents the density of states of a normal metal, while the blue the density of states of a BCS superconductor. Central, state-less superconducting gap of 2Δ is the characteristic property of superconductivity.

The density of states (DOS) is shown in figure 2.6, where the states below 0 energy are already filled. In the ground state, the energy states are therefore populated up to $-\Delta$, and all excitations are raised above the gap Δ, leading to the expected divergence of the density of states in the vicinity of $E = \Delta$.

2.2.5 Proximity effect

To be perfectly precise, the superconductivity investigated in this thesis is not strictly speaking traditional. Typical distances between two electrons involved in the interaction can be estimated by considering Fermi velocity of electrons in a metal ($\sim 10^6$ m/s) and typical times it takes for the lattice to distort ($\sim$ 100 fs), to be on the order of hundreds of nm. This distance is also called the coherence length ξ. When a piece of a superconducting material is in contact with a piece of normal metal, the density of Cooper pairs cannot abruptly drop to zero upon transition from the superconductor to the metal. The electron correlation thus extends within the normal metal on the scale of ξ, inducing weaker superconductivity. This is known as a proximity effect, and it plays a vital role within Majorana physics, as it allows for the combination of strong spin-orbit coupling and superconductivity.

2.3 Gate-Based Reflectometry Readout

Several different techniques can be employed for a readout of the quantum state in solid-state systems. One such way is by investigating the electron transport by measuring the current or differential conductance through the system. A downside of this technique is that the system must be coupled to fermionic reservoirs, which are in itself a significant source of decoherence and in the case of a superconducting charge island, quasiparticles. Additionally, single-electron transitions cannot be resolved, an important limiting factor when probing local internal processes. Another approach that allows for selective and local measurements of single tunnelling events from a quantum dot is by capacitively coupling a Quantum Point Contact (QPC) or a Single Electron Transistor (SET) to the dot, and measuring the radio-frequency (RF) conductance through it [38, 39]. By carefully tuning such devices, tunnelling charges can be probed directly. As opposed to the traditional DC conductance measurements, the system can be operated and investigated in a so-called *floating regime*, i.e. entirely decoupled from the leads. However, as each sensor needs to be in close proximity to the quantum dot, this method proves to have a disadvantage of scalability. Reflectometry provides a way of alleviating these problems and can serve as a compelling technique enabling scalable and high-fidelity readout of qubits in solid-state systems. In particular, in the dispersive limit, where the resonator and qubit transition frequency are far detuned, *dispersive gate sensing* (DGS) allows for the measurement of the tunnel coupling strength and events in the system.

2.3.1 Reflectometry

By capacitively coupling an LC resonator tank circuit, with some inductance L, and capacitance C_0 to one of the gates of the system as in Fig. 2.7a, the technique of reflectometry can be used to discern different states of the system. In particular, the idea behind the reflectometry is as follows: the resonator is coupled to a double quantum dot, which can be effectively modelled as a system of capacitors and resistors. Any coherent single-electron tunnelling events will slightly perturb the bare capacitance of the system by some shift C_p. In our devices, the resonators are transmission line resonators (and will be further introduced in Section 3.2), which for a large sample impedance can be modelled as an effective LRC circuit with all components in parallel with one another (see Fig. 2.7a). In the frequency domain, the resonators impedance $Z(\omega)$ can be characterised by contributions of the inductive, capacitive and resistive components as[6]

$$Z_{RLC}(\omega) = \left(1/i\omega L + i\omega C + 1/R\right)^{-1}, \tag{2.18}$$

---

[6] In many electronics books and texts, the letter indicating the imaginary number is j rather than i. In this text, we will simply keep to the conventions from the realm of mathematics, and use the latter.

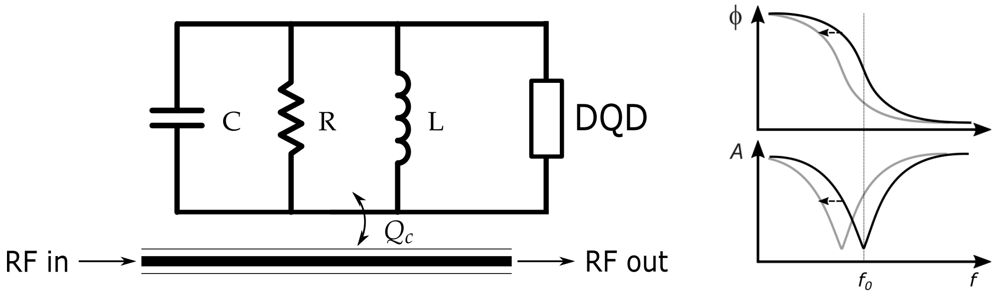

(a) (b)

FIGURE 2.7: **(a)** An LRC resonator scheme a notch geometry, where it is coupled to the transmission line with some coupling factor κ_{ext} [40], for large device impedance. Such geometry allows for multiplexed readout of multiple resonators. The system is measured in transmission S_{21}, with the resonance appearing as a dip in transmission coefficient spectrum. **(b)** Charge hybridisation shifts the resonator's characteristic resonant frequency, which results in a shift in amplitude A and phase ϕ of the probe signal, relative to the response on resonant frequency.

with C being the total capacitance of the system $C = C_0 + C_p$ and R some internal resistance. The characteristic resonance frequency of this resonator is $\omega_0 = 1/\sqrt{LC}$, which reduces the impedance in Eq. 2.18 to R. Therefore the shift in C_p will directly correspond to the shift in the resonance frequency

$$\Delta\omega = \frac{1}{\sqrt{L(C_0 + C_p)}} - \frac{1}{\sqrt{LC_0}} \tag{2.19a}$$

$$\sim -\frac{\omega_0 C_p}{2C_0}, \quad C_p \ll C_0. \tag{2.19b}$$

The last simplification can be done as the perturbing shift is expected to be much smaller than the capacitance of the resonator.

The carrier signal at ω_0 is then off-resonance with the LC circuit, which shows as a change in both magnitude as well as in phase of the reflected signal, as depicted in Fig. 2.7b. To calculate each, one investigates the *voltage reflection coefficient* Γ as the ratio between the incident and reflected RF voltage V_i and V_r respectively, $V_r/V_i = |\Gamma|e^{i\Delta\phi}$ [41]. Its magnitude can be expressed in terms of effective resistance R and reactance X

$$|\Gamma| = \frac{\sqrt{(R - Z_0)^2 + X^2}}{\sqrt{(R + Z_0)^2 + X^2}} \tag{2.20a}$$

$$= \frac{\omega - \omega_0(1 - i/2Q)}{\omega - \omega_0(1 + i/2Q)} \tag{2.20b}$$

where $Z_0 = 50\Omega$ is the standard impedance of the transmission line. Assuming the system is probed at the resonator's bare frequency (the detuning $|\delta| \equiv |1 - \omega/\omega_0| \ll 1$), the expression can be simplified by expressing the reactance $X = \omega L - 1/\omega(C_0 +$

C_p). The Eq. 2.20b denotes the same coefficient in the frequency domain, where $Q = \omega_0/\kappa_{ext}$ is the quality factor of the resonator, with κ_{ext} the resonators external coupling rate to the transmission line, which can be controlled through a coupling capacitor. Clearly on resonance, the coefficient yields $\Gamma(\omega_0) = -1$, whereas for any small magnitudes of detuning $\Delta\omega$ away from it, the phase shift is

$$\begin{aligned} \Delta\phi =& \arg(-1) - \arg(\Gamma(\Delta\omega)) = \\ =& \pi - \operatorname{atan2}\left(\frac{\kappa_{ext}\Delta\omega}{\Delta\omega^2 + (\kappa_{ext}/2)^2}, \frac{\Delta\omega^2 - (\kappa_{ext}/2)^2}{\Delta\omega^2 + (\kappa_{ext}/2)^2}\right), \end{aligned} \tag{2.21}$$

with atan2 being the two argument arctan function.

2.3.2 Parametric Capacitance

The shift in capacitance C_p, responsible for the shift in resonance frequency is called a *parametric capacitance*. Its physical origin can be explored by investigating the differential capacitance associated to the DQD as seen from the coupled gate voltage on the second dot V_{g2}, as in figure 2.7a

$$C_{diff} = \frac{d(Q_1 + Q_2)}{dV_{g2}}, \tag{2.22}$$

with Q_i the net charges on the respective dot [42]. These charges can be determined by considering the average total existing charge on the island $-e\langle n_i \rangle = C_{gi}V_{gi} - CV$, the charge induced by the gate electrode and the mutual effects between the two dots, which can be neglected in the weak coupling limit, where the mutual capacitance is small compared to the total self-capacitance of each dot. The brackets denote a quantum expectation value of the number of electron on the dot i, which in the zero temperature limit we can take as being the expectation value in the ground state. This leads to

$$Q_1 + Q_2 = e(\alpha_1\langle n_1 \rangle + \alpha_2\langle n_2 \rangle) + (\alpha_1 C_s + \alpha_2 C_d)V_{g2}, \tag{2.23}$$

with α_i the lever arm on the dot i, defined as in 2.1, $\langle n_i \rangle$ the average electron number on the dot i, and V_{g2} the gate voltage applied to the dot 2. Inserting Eq. 2.23 into Eq. 2.22 yields the two components of the differential capacitance; one independent of the gate voltage describing the geometry of the system, which we shall conveniently call the *geometric* or *classical capacitance* C_{geom}, and one dependent on it - *parametric* *capacitance* C_p:

$$\begin{aligned} C_{diff} =& (\alpha_1 C_s + \alpha_2 C_d) - e\left[\alpha_1 \frac{d\langle n_1\rangle}{dV_{g2}} + \alpha_2 \frac{d\langle n_2\rangle}{dV_{g2}}\right] \\ =& \underbrace{(\alpha_1 C_s + \alpha_2 C_d)}_{C_{geom}} - \underbrace{e\alpha' \frac{d\langle n_2\rangle}{dV_{g2}}}_{C_p} \qquad (near\ ICT) \end{aligned} \tag{2.24}$$

with $\alpha' = (\alpha_2 - \alpha_1)$. Near the interdot charge transition (ICT), the exchange of electrons happens between the two dots, so $d\langle n_1\rangle/dV_{g2} = -d\langle n_2\rangle/dV_{g2}$. This approximation, however, becomes less valid away from the interdot transition, as one of the dots could lose or gain an electron, without affecting the charge state of the other dot. Notably, parametric capacitance depends on the *change* in the statistical average of the charge on the island. For small shifts around the Coulomb resonance, dV_{g2}, the energy change is $d\epsilon = -e\alpha' dV_{g2}$, which allows us to express the parametric capacitance in terms of the local density of states $\rho = d\langle n_2\rangle/d\epsilon$. As the expected average number of electrons on a dot can vary both adiabatically and nonadiabatically, which manifest itself as two different contributions to the parametric capacitance - quantum capacitance C_q and tunnelling capacitance C_t.

2.3.3 Quantum and Tunnelling Capacitance

The adiabatic transition occurs when two quantum levels are hybridised, and the contribution to the parametric capacitance resulting from the delocalisation between the two quantum dots, is called *quantum capacitance* [42–44]. Near the interdot transition, at the anti-crossing between two charge states $|n+1, m\rangle$ and $|n, m+1\rangle$, the electron does not have a well-defined position with respect to either dot, but is rather in superposition between occupying the first or the second dot, causing the average electron number to vary. The Hamiltonian for a DQD two-level system can therefore be expressed as

$$H = t_c \sigma_z + \frac{\epsilon}{2}\sigma_x, \tag{2.25}$$

with ϵ the detuning from the resonance, t_c the interdot tunnel coupling energy, accounting for the hybridization of the discrete charge states, and σ's the Pauli matrices ($\hbar = 1$). The corresponding energy eigenstates are $E_{g,e} = \pm[(\epsilon/2)^2 + |t_c|^2]^{1/2}$, assuming no orbital degeneracy. Quantum capacitance of the system in the ground state, can be expressed as [45, 46]

$$C_q = (e\alpha')^2 \frac{\partial^2 E_g}{\partial \epsilon^2}. \tag{2.26}$$

We can see that the quantum capacitance arises from non-zero curvature of the energy bands! For zero detuning $\epsilon = 0$ (at avoided crossing), where the curvature of the eigenenergies of the system is maximum, so is the quantum capacitance, which

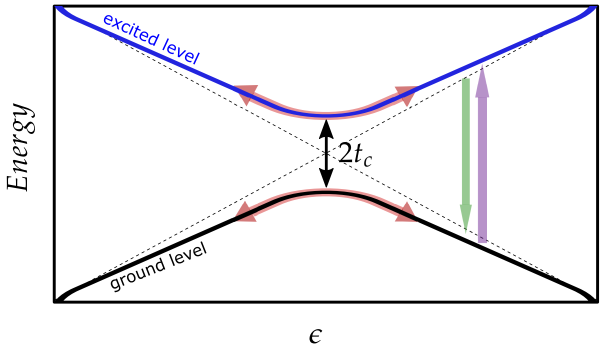

FIGURE 2.8: Explanation of processes related to quantum capacitance (the red arrows), and to tunnelling capacitance (in green and purple, relaxations and excitations). Additionally, Sisyphus resistance R_{Sis} is sometimes used to describe additional dissipation of the system, which arises from the interaction with the phonon bath. The width of the anticrossing is twice the interdot tunnel coupling energy, accounting for the hybridization of the discrete charge states. By sending an RF pulse to the sample, we are causing an oscillation around the detuning.

simplifies to [43, 45]

$$C_q\Big|_{\epsilon=0} = \frac{(e\alpha')^2}{4|t_c|}, \tag{2.27}$$

which reveals that the quantum capacitance has a direct correspondence to the state hybridisation parameter of the system [47].

Tunnelling capacitance, on the other hand, does not require level hybridisation. The charge can jump between band nonadiabatically, for example through relaxation or thermal excitation. It, however, only arises when the rates of excitation and relaxation are on par with the probe frequency. Assuming that the dominant source of charge excitation and relaxation is from phonons, we write $\Gamma_e = \Gamma_c n_p$ and relaxation $\Gamma_r = \Gamma_c(1 + n_p)$, with Γ_c the charge relaxation rate and $n_p = [\exp(-\Delta E/k_b T) - 1]^{-1}$ the number of phonons described by Bose-Einstein distribution [46]. The two possible transitions, responsible for two possible capacitance contributions can be summarised as in Fig. 2.8.

2.4 Dispersive Readout SNR

Identifying a poisoned state of the system from an unpoisoned one effectively translates to discriminating between a finite tunnel coupling and one that is nearly zero. As explained in the section above, the tunnel coupling produces a state-dependent frequency shift as a result of coherent single-electron tunnelling. The resonator is probed with the RF voltage applied to the gate V_{g2} (to agree with figure 2.7a). To resolve different responses, one can look at the in-phase (I) and quadrature (Q) components of the signal, and plot the response in the IQ space. If the attempt is to discriminate between two possible responses of the resonator, i.e. two possible frequencies giving rise to two possible phases, we can define the 'measure of quality' of the signal, as *signal-to-noise ratio* (SNR) related to the square root of the ratio between the signal power and noise power[7]

$$SNR = \sqrt{\frac{P_S}{P_N}} \sin(\Delta\phi/2). \tag{2.28}$$

Here, $\Delta\phi$ is the phase shift and $P_S = \bar{n}\kappa_{ext}\hbar\omega$ is the signal power, with $\bar{n}$ being the number of circulating photons in the resonator. The noise power $P_n = k_B T_N / T_m$, is described in terms of the measurement time T_m and the temperature of the noise of the system T_N. Since typically the Gaussian distribution of the two signals in the IQ plane is assumed, we can associate the SNR with assignment fidelity through complementary error function $P_{inc} = 1/2\,\mathrm{erfc}(SNR/\sqrt{2})$, assuming normalised Gaussian distribution.

Looking at Eq. 2.28, it might seem that an easy path towards a higher signal-to-noise ratio is simply by increasing the readout power. However, An important limitation to acknowledge in order to maximise the SNR, is the fact that by increasing the readout power the population of the excited state is increased through driving[8]. This results in an incoherent mixture, reducing the contrast, as the quantum capacitances of the excited and ground state are exactly opposite. In order to roughly estimate the dynamics, we can employ a toy model using the Hamiltonian in Eq. 2.25[9]. Driving implies modulating the detuning ϵ around degeneracy with some frequency ω

$$\begin{aligned} \epsilon = \epsilon(t) = \epsilon_0 \cos(\omega t) =& \frac{E_C C_g V_{rf}}{e} \cos(\omega t) \\ =& e\alpha V_{rf} \cos(\omega t), \end{aligned} \tag{2.29}$$

with V_{rf} the maximum amplitude of the gate voltage around the degeneracy. In the rotating frame, the full Hamiltonian reads:

$$\tilde{H} = \frac{\Delta}{2}\sigma_z + \frac{\Omega}{4}\Big(\sigma_x + \cos(2\omega t)\sigma_x - \sin(2\omega t)\sigma_y\Big), \tag{2.30}$$

with detuning from the resonance $\Delta = \tau - \omega$, with $\tau = 2t_c/\hbar$, and $\Omega = e\alpha V_{rf}$ is the on-resonance Rabi frequency. We can further make some reasonable approximations. By investigating the eigenstates of the time-independent part of the Hamiltonian, assuming that all fast-rotating terms lead to random phase jumps rather than coherent processes, we can estimate the time-averaged population in the ground state p_{gs}. We find

$$p_{gs} = \frac{\Omega^2}{\Omega^2 + (\Delta - \Omega_{eff})^2}, \tag{2.31}$$

---

[7] Sometimes, SNR is defined as the square value of 2.28. Here we chose this version, as it is equal to the reciprocal of the coefficient of variation.

[8] From experiments we know that at high readout powers the frequency shift vanishes [48].

[9] This approach might not be as correct in principle as the full input/output theory modelling the system of the resonator and the dot in the Jaynes-Cummings framework [49], but it still gives good agreement with the current experimental data.

where $\Omega_{eff} = \sqrt{\Omega^2 + \Delta^2}$ is the effective detuned Rabi frequency. A more 'radical' approach where we assume that the state vector randomly jumps between the extreme values of the ground state population, p_{gs} can be expressed as half the maximum of the excited state probability from a detuned Rabi oscillation, $p_{gs} = 1 - \Omega^2/\Omega_{eff}^2$. A full and detailed derivation is given in Appendix A. To summarise: the dependence of the SNR on power results from the contention between the increase in signal, and the excitation in the double dot, which reduces the contrast. The optimum is reached at the point where the improvement gained from larger accuracy in the IQ plane falls short to the diminishing frequency shift.

Chapter 3

Experimental Setup

In this chapter, the experiment is described, as well as what is needed for its realisation, starting from the macroscopic equipment, such as cryogenic refrigerators and DC and RF wiring schemes, down to the microscopic double quantum dot device and the resonator chip design.

3.1 Measurement Setup

To ensure the quantum nature of our devices, superconductivity and good electric transport properties, and to make sure Coulomb blockade is present, the experiments need to be performed at low temperatures. Nowadays, the majority of condensed matter experiments operate in the temperature regime of millikelvins, which necessitates closed and thermally isolated systems. At the same time, however, probing the system demands some information be exchanged with the environment. This is usually done through the application of DC voltages to the system and reading the conductance, or in reflectometry experiments, a microwave RF signal.

3.1.1 Dilution Refrigerator

The largest physical object directly involved in the experiment is a Bluefors dilution refrigerator, responsible for ensuring operational base temperatures of around 10 - 20 mK. The entire cooling process is done in stages, which is reflected in the internal structure of the fridge. First, cool-down to roughly 4 K is achieved via pulse-tube vacuum pump refrigeration - a process known as *dry cooling*[1]. The final cooling stage utilises endothermic properties achieved when two isotopes of helium, ^{3}He and ^{4}He, are mixed in the so-called *mixing chamber* (MC). This mixture then separates into a dilute phase where the lighter almost pure ^{3}He floats on top of the diluted heavier counterpart. By pumping the ^{3}He phase away, the remaining phase is pushed out of an equilibrium state, which in turn moves the ^{3}He from pure into the dilute phase. This process, however, extracts the temperature from the mixing chamber, effectively cooling it down. Finally, the ^{3}He gas is pumped out of the fridge through

---

[1] Alternatively, a *wet fridge* is one where the environment of the fridge is surrounded by liquid nitrogen and liquid helium. Within QuTech laboratories, both can be found, but for the experiments described in this thesis, a dry system is used.

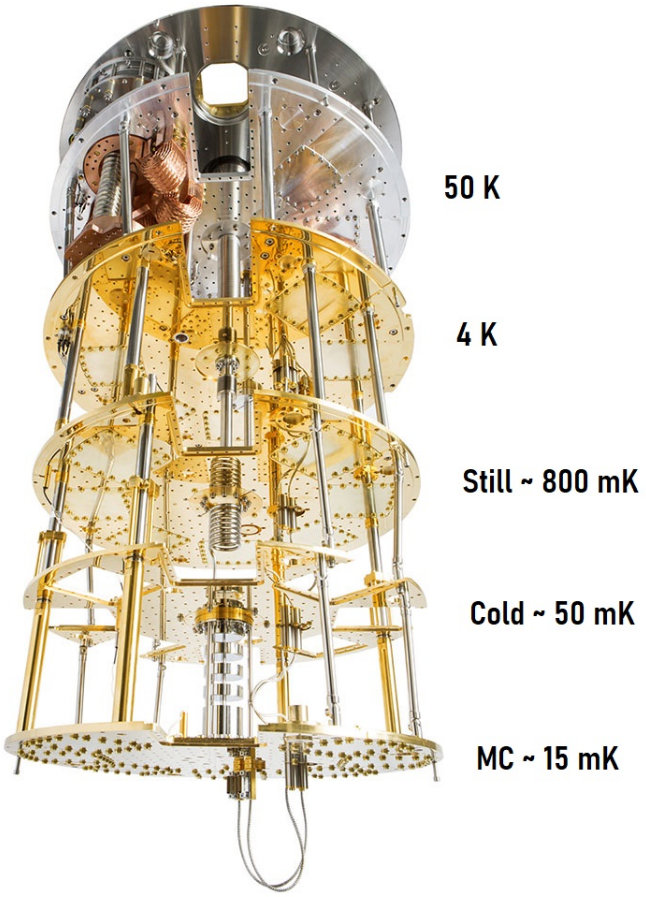

FIGURE 3.1: The innards of a Bluefors dilution refrigerator, similar to the one used. Different plates corresponding to different working temperatures indicated on the figure.

cold traps, which trap contaminants in the mixture, before it is at high pressures condensed again, completing the loop [50, 51]. Internally, the fridge consists of several plates (as in Fig. 3.1), corresponding to sequentially lower operational temperatures down the refrigerator: 50K plate, 4K plate, still (800 mK), cold (50mK) and finally the MC plate at roughly 15mK, where the sample is located. Stages itself are held together with thermally isolating fibreglass rods. The sample itself is mounted onto a "cold finger", the top of the probe loaded into the fridge, which is attached to the MC, and encompassed by a printed circuit board (PCB), providing bonding wires between the lithographically defined lines on the sample, and the external electronics within the fridge. In our experiment, the probe can be raised into the refrigerator from below and is kept in thermal contact with the chamber, which provides for the cooling of the device.

3.1.2 Electronics

To probe the system, and conduct the experiments, proper wiring is of fundamental importance. All signals used to operate and conduct experiments on the device originate from the electronics at room temperatures, and are thus very noisy. To that effect, the electron temperatures can be much larger than the base temperatures of the fridge. For that reason, it is vital to attenuate and filter the signal on the way into the cryogenic setup and amplify on the way out. In our case, two different parts of wiring are used and must be discussed: RF and DC.

To tune the system and change the chemical potential of the double dot system, DC voltages controlled from a set of Digital to Analogue Converters (DACs) are routed to the correct fridge DC lines by the matrix module. To restrain the effects of the room temperature noise, DC lines are attenuated and heavily filtered using QDevil RC filters.

RF signals needed for our experiment, on the other hand, come in two flavours. The signal can be both generated and read out by either Rohde&Schwartz vector network analyser (VNA), or a QuantumMachines OPX. The VNA is best suited for frequency sweeps, and as it can output signals in the range of the resonant frequencies of our resonant circuit (GHz), no up- or down-mixing is required before entering the fridge. The OPX, on the other hand, cannot output signal in that frequency range, so the OPX frequency ω_{OPX} needs to be up-mixed with a signal from a local oscillator (LO) at ω_{LO}, creating a signal at $\omega_{LO} - \omega_{OPX}$[2]. This up-mixed signal is then sent in the refrigerator and is finally downconverted with the same LO to obtain the component of the signal at ω_{OPX}, which is then routed into the OPX for receiving and processing the IQ data (the external wiring depicted in 3.3a). The main asset of OPX for the needs of the experiments presented in this thesis is the integrated specialised field-programmable gate array (FPGA), which allows for the manipulation and processing of the data with nanosecond precision, and its ability, to measure with integration times (pulses) as short as a μs. All key constituents for performing time-resolved measurements with μs resolution.

The setup of the RF wiring once inside the fridge is shown in Fig. 3.3b. Once the signal enters the fridge, it is further heavily attenuated to reduce the noise, and filtered using low pass filters and eccosorb, before reaching the puck with the sample. After the signal passes through the puck, it is fed into the directional coupler, which makes sure that the attenuated component is transmitted to the PCB, while the reflected signal almost in its entirety to the output port. The signal is then amplified again, twice at cryogenic temperatures, using Lincoln Labs Travelling Wave Parametric Amplifier (TWPA) [52] and Cryogenic high electron mobility transistor (HEMT) amplifier, and again at room temperatures. Using 50 Ω coaxial cables, the RF signal is guided to either OPX or VNA, whereby comparing the in-phase (I) and quadrature (Q) components of both signals, the amplitude (A) and the phase (ϕ) information of the signal can be extracted as $Ae^{i\phi} = I + iQ$.

---

[2] The mixing process in fact also outputs the original LO frequency as well as their sum, but the mixer is calibrated to reduce the other two signals to 0.

3.2 The Quantum Dot Device

Finally, at the coldest point in the core of the cryogenic refrigerator, we find the sample. For the experiments in this thesis, two devices have been fabricated and measured. Both contain semiconductor and superconductor quantum dots, thus often simply called hybrid devices. For the experiments in this thesis, quintuple dot systems were defined in an InAs nanowire (NW). One such device, based on the same design as one of the devices used in the experiment, is pictured in Fig. 3.2. The nanowire is deposited on an intrinsic silicon wafer with roughly 20 nm of SiNx dielectric layer. The aluminium shell is epitaxially grown on two of the facets of the nanowire and is removed using wet etching everywhere, except for an approximately 1 μm wire segment (1.9 μm for the second device[3]). At temperatures below the critical temperature of aluminium, this wire segment enters a superconducting phase due to the proximity effect.

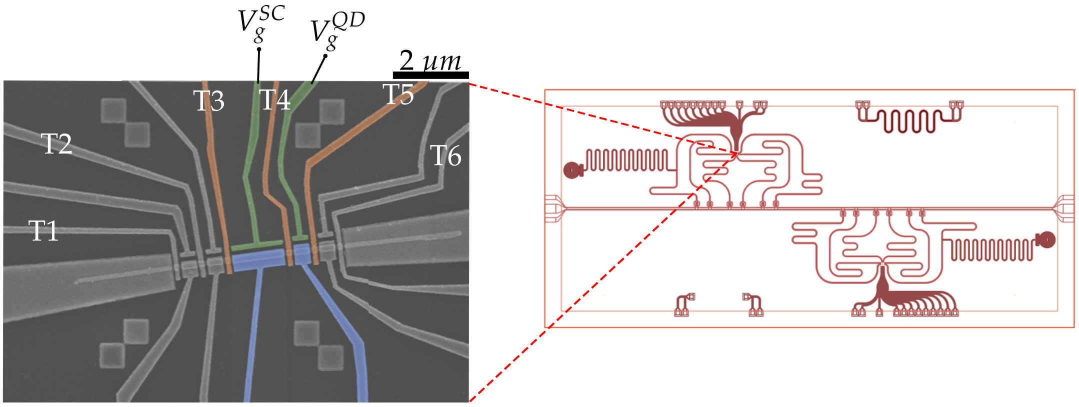

FIGURE 3.2: An SEM image of a quintuple dot device based on the same design as the devices in the experiment. For the purposes of this experiment, only the middle superconducting dot, and one of the neighbouring dots are used, defined using tunnel gates T3, T4 and T5 (coloured orange), as well as the side gates (in green), and top gates (in blue). By applying a negative voltage to T3 and T5, the rest of the system can be effectively "pinched-off". The device is placed within an on-chip resonator, depicted on the right side of the figure, with a central transmission feedline with hanging resonators. The first resonator from each of the two sets is connected to the bias-tee filter, allowing for DC biasing. Note that the resonator architecture allows for two devices to be mounted simultaneously (one above and one below the feedline).

Different quantum dots and the tunnelling barriers between them are controlled using tunnel gates T1-6 (coloured orange in Fig. 3.2), lying on top of the nanowire. They are separated from the nanowire by a relatively thin 10 nm AlOx dielectric layer formed with atomic layer deposition, to ensure large lever arm. These gates can be used to "pinch-off" the coupling to the leads and tune the interdot coupling between the dots. In this manner, we can modify our system into several different arrangements. For the first (second) device in our experiment, we apply large (-2 V) electric voltage on the two side tunnel gates T3 and T5 (-1.3 V on T2 and T4 on the second device), leaving us with a hybrid double quantum dot, entirely decoupled

---

[3] Estimated as the distance between the tunnel gate inner edges

from the leads. In blue, another set of 'top' or 'wrap' gates[4] can be used to define chemical potential on each dot. However, in our experiment we control the chemical potential, and thus the charge occupation of each dot, using the side gates (coloured orange in Fig 3.2), while we use the top gates for resonator-based sensing. Having the DC and RF gates completely separated is advantageous, as no additional bias tees are needed to combine the RF and DC signals. The one exception is the bias tee used for the source-drain bias. Additionally, compared to the side gates, wrap gates have very high lever arms (as they are closed to the nanowire), which translates into higher SNR.

To employ reflectometry, the sample is implemented within an on-chip superconducting coplanar waveguide (CPW) resonator [53], depicted in the right half of Fig. 3.2 [54]. The resonator chip consists of the central transmission line, also called the feedline, with resonators of different characteristic resonant frequencies capacitively coupled to it via a hanger geometry[5]. Experimentally, we are interested in the state-dependent reflection coefficient of the resonator (S_{11}), which is measured indirectly via the transmission coefficient (S_{21}) of the feedline circuit. In this geometry, the resonances can be seen as an overall dip in the transmission spectrum, as a function of frequency.

---

[4] As they lie on *top* of the nanowire/are *wrapping* the nanowire

[5] Resonators are "hanging" off the central feed line via a capacitive coupling element.

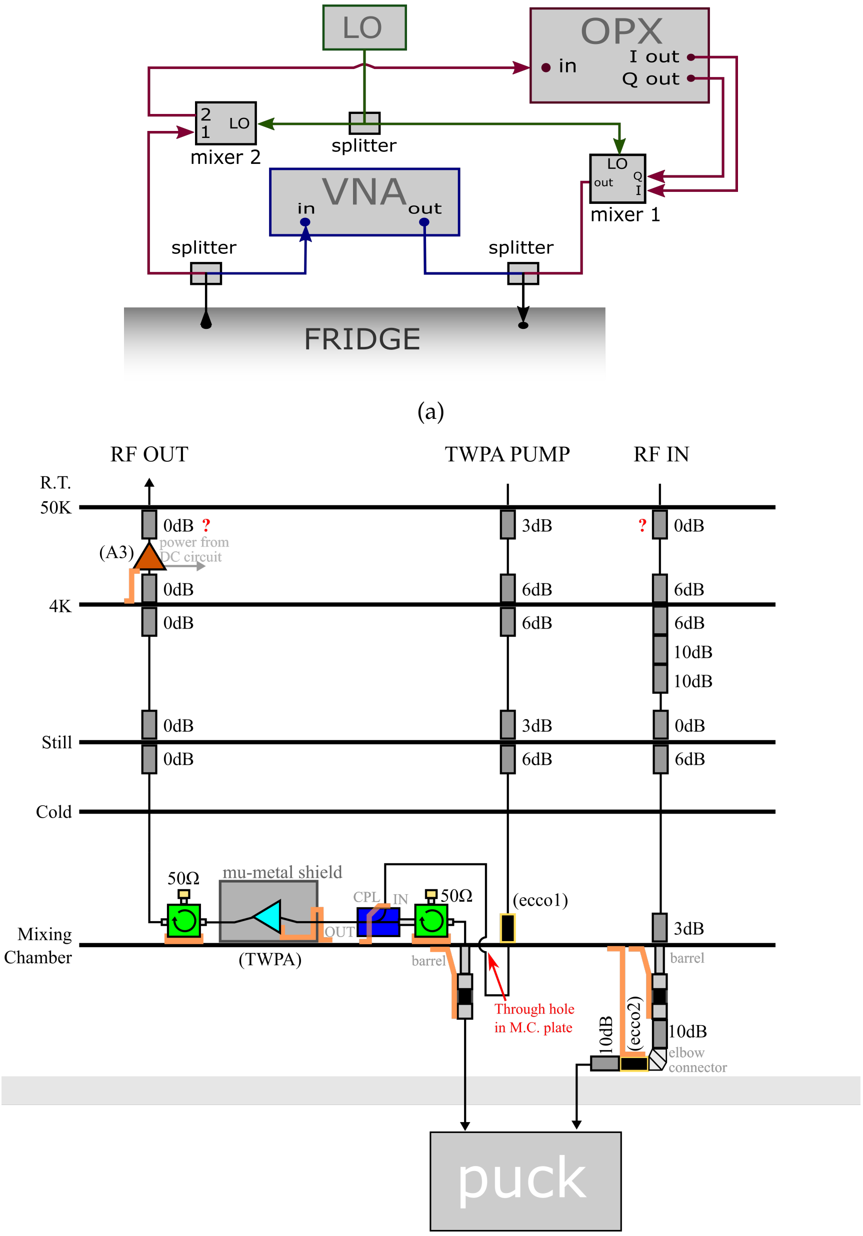

(a)

(b)

FIGURE 3.3: The RF wiring of the setup. **(a)** Both VNA and OPX measurements can be performed using the setup. In the case of OPX, the output frequency needs to be upmixed using a local oscillator. **(b)** RF attenuation and wiring in the fridge. The incoming RF signal is heavily attenuated using XMA Cryogenic attenuators (roughly additional 61 dB of attenuation) and filtered using K&L 10GHz low pass and Eccosorb filters (attenuating additional 1.6 dB per GHz) before entering the puck and reaching the sample. The attenuators are in thermal contact with the corresponding stages of the refrigerator to ensure thermalisation of the cable's inner conductor, thus reducing the noise without further creating it. On the way out, the signal is again filtered before passing through Quinstar circulator (green) and Krytar directional coupler (blue), both thermalised using copper wires or brackets. The signal is then amplified again, twice at cryogenic temperatures, using a Lincoln Labs Travelling Wave Parametric Amplifier (TWPA) and Cryogenic high electron mobility transistor (HEMT) amplifier, and again at room temperatures. Although 0 dB attenuators might seem redundant, they ensure thermalisation with the inner conductor of the cable.

Chapter 4

Experimental Results

With all the fundamentals set in place, we can now get to work, and design and conduct the experiment, in which we hope to get a better understanding of the dynamics of quasiparticles in superconducting systems.

4.1 Quasiparticle Poisoning

Before introducing the practicalities of the experiment, it is vital to place the experiment in context. Quasiparticle poisoning is a very known limitation of superconducting devices and has as such been thoroughly investigated in the past by scrutinising metallic superconductors [20–22], as well as semiconductor-superconductor hybrid structures [23–25]. In most cases, the population of odd relative to even states of the SC (an excess QP on the island, or no excess QP on the island, respectively) was investigated by either investigating the charge parity effects in SC [55], properties of supercurrent [56], or in recent attempts by employing radio-frequency reflectometry [20, 57, 58], analogous to the method presented in this thesis. To investigate the dynamics of QPs, time-resolved scans are typically carried out, with the state-of-the-art technology allowing for probing the characteristics of poisoning events on a microsecond scale. For the purpose of our experiment, we probe the system using time-domain RF reflectometry on a microsecond resolution, an established technique previously implemented in investigating quasiparticle dynamics [20, 57, 59, 60].

As sizes, materials and types of superconducting samples used vary significantly between different experiments, it is difficult to make any concrete claims or predictions about the rates of quasiparticle generation and relaxations, or their density in the samples presented in this thesis. For a SC charge island in contact with metallic leads, observed quasiparticle lifetimes[1] are usually on the scale of few to tens of microseconds [20, 24, 25, 57], with their densities saturating at low temperatures to

---

[1] The definitions of a "quasiparticle lifetime" often slightly vary based on the methods used.

around 10 - 60 $/\mu m^3$ [19, 58][2]. This is within the experimental scope of this experiment.

The origin of QPs in the system can be tracked to different mechanisms. They might come from the surrounding environment (for example stray EM radiation might excite an electron on a nearby quantum dot to tunnel onto the island), they might be located within the topological subgap states, or might be internally excited through external perturbations or phonons within the island itself. A phonon with energy larger than twice the superconducting gap could break a Cooper pair, resulting in two quasiparticles with opposite spin and momenta. Here we are mostly interested in the last two mechanisms, the quasiparticle poisoning dynamics that happen within the island. To limit poisoning to the events of interest, we can exponentially suppress poisoning due to the external quasiparticles by introducing a gapped segment of the wire, while keeping electrical contact with the leads [26]. In the experiments presented in this thesis, we take this a step further and decouple the charge island from the surroundings completely and probe it solely using RF reflectometry rather than conductance measurements. This way, we eliminate a need for the leads, which are in themselves potential sources of quasiparticles.

This is the first time *time-resolved* studies of quasiparticle poisoning have been conducted in a superconductor-semiconductor hybrid system, which is completely decoupled from the leads. This investigation allows for all detected quasiparticle poisoning events to be associated with the processes related to the SC itself.

4.2 Description of the experiment

To measure the electron-tunnelling events that could be related to quasiparticles on the island, the following strategy is employed: an empty energy level of a quantum dot is brought in resonance with an energy level on the island expected to host

---

[2] We need to keep in mind, that these experiments were performed in different systems with electrical contact to the leads, with slightly different energy scales from the ones characteristic of our devices. For example, [57] reports different gap profiles of otherwise identical devices lead to strikingly different trap properties, with smaller gaps trapping the QP's for a longer time.

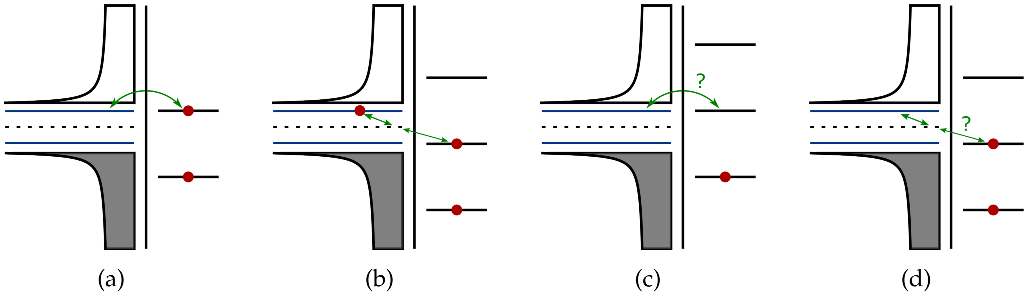
(a) (b) (c) (d)

FIGURE 4.1: The different transitions corresponding to different peaks on double-dot CSD. See Appendix B for details.

quasiparticles, where we fix the chemical potentials and repeatedly measure the resonator response. If no quasiparticles are present, then no tunnelling should occur, while if there is an excess of electrons on the island above the gap, the QPs can tunnel back-and-forth between the two available levels. This can be visible as the shift in the magnitude and phase (or equivalently the I and Q signal components) of the RF signal reflected from the system. Due to particle-hole symmetry in the superconductor (where creating a QP at positive energy is equivalent to annihilating a QP at negative energy), we expect two energy tunings allowing for that transition (as illustrated in Figs. 4.1c and 4.1d). As the superconductivity in our sample occurs via the proximity effect, we might expect a subgap state $2\widetilde{\Delta}$ away from charge transitions, with $\widetilde{\Delta}$ the lowest single-particle energy state (a subgap state, shown as a blue line in Fig. 4.1).

By carefully investigating possible tunnelling events between the SC and a normal QD in a floating regime, we can thus predict how quasiparticle poisoning events should imprint themselves on the charge stability diagram of the system. A complete and detailed description of the processes resulting in a CSD as the one in Fig. 4.2b, together with derivations of the spacings of the parallel lines, is given in Appendix B.

First, operating the hybrid double dot in a floating regime causes the CSD to lose the grid-like structure, resulting rather in parallel lines, which become unevenly spaced when one of the dots is superconducting, and even total charge number is preferred on the island (Fig. 4.2b). This results in broader even regimes with spacing $S_e/\alpha = E_c^{SC} + E_c^{QD} + 2\widetilde{\Delta}$, and narrower odd regimes with spacing $S_o/\alpha = E_c^{SC} + E_c^{QD} - 2\widetilde{\Delta}$. Combined with the energy spacings of the QP tunnelling configurations, we expect the "shadow" peaks, to lie in the middle of the even Coulomb blockade regime, with the same odd-regime spacing. In other words, the expected shadow peaks should reside exactly where the 1e periodic peaks would be if you killed superconductivity. This feature has been experimentally observed before in hybrid devices conductance measurements [24, 55, 61], but never in reflectometry measurements.

Such CSDs have been previously reported within our group (figure 4a) in [62]), but no additional "shadow" lines indicating QP transport was visible. Arguably, however, it would be too early to claim no quasiparticle events occurred. The best we can claim is that *at the time resolutions* and integration times used in the experiment, no tunnelling events indicating the quasiparticle poisoning could be visible. However, a CSD of the hybrid double dot in the floating regime (Fig. 4.2a), measured before proper shielding was in place, shows 1e periodicity in gate voltage[3]. The most probable explanation is that external high-frequency radiation was incident on the sample, which caused a steady-state, non-zero number of quasiparticles

---

[3] It could be that the spacing in the diagram was, in fact, $2e$, but based on the known values of the lever arms we ruled that option out.

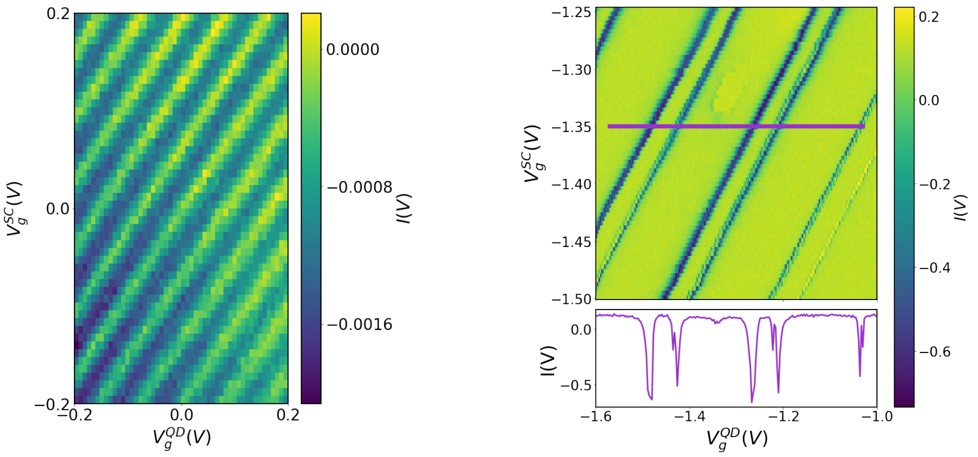

(a)

(b)

FIGURE 4.2: **(a)** 1e periodic signal, hinting at non-zero number of quasiparticles on the island. This was sufficiently fixed using filters and protecting the sample from high-frequency radiation, and the 2e periodic response as in **(b)** was restored. **(b)** An even-odd spacing in the CSD indicates the preference for an even number of charges on the island, a characteristics of superconductors. The difference in the even and odd peak spacing $S_{even} - S_{odd}$ is a direct measure of $\widetilde{\Delta}$.

on the island. After proper shielding was in place[4], the 2e periodicity (as in Fig. 4.2b) was restored.

To more precisely probe individual quasiparticle dynamics on the island, a single line-cut of the diagram in Fig. 4.2b is measured (along the purple line), which experimentally corresponds to sweeping the voltage of the normal QD gate. What we obtain is a single line-cut (bottom of Fig. 4.2b), which allows us to more thoroughly investigate the spectrum, looking for a potential third and fourth peak. To investigate time dynamics, we integrate over 1.000 and 30.000 successive 1 μs pulses. This allows us to produce a 'time-map' of tunnelling events of microsecond resolution.

4.3 System Tune-up and Characterisation

Before presenting the proper experimental results, it is useful first to discuss the steps needed to tune the device, such that the experiment can take place. To do so, we make use of both DC and RF measurements. In particular, we want to define a double quantum dot decoupled from leads with an intermediate interdot coupling (1), gain some information about the energy scales and energy values of the system (2) and characterise the resonant frequency for each dot's resonator (3).

In order to define floating quantum dot systems, it is necessary to investigate the ranges of the tunnel gate voltages T3-5 (T2-4 in the second device), that either completely restricts the flow of electrons or allow for weak tunnelling across them.

---

[4] More precisely, the addition of bandpass and eccosorb filters, circulators, and the directional coupler. Afterwards, all the seams of the copper sample box were we sealed off using copper tape, surrounded by eccosorb pads and finally wrapped in Mylar foil. The setup in Fig. 3.3b shows the already shielded circuit)

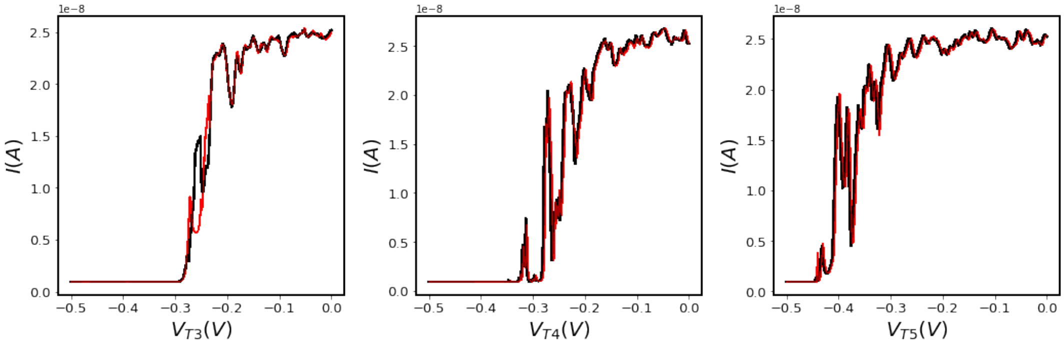

(a) (b) (c)

FIGURE 4.3: By investigating the current between two dots, pinch-off curves for each of the gates can be plotted, and we can determine what voltage provides weak tunnelling across them, and what regime completely decouples two neighbouring dots. An example of such curves for **(a)** T3, **(b)** T4 and **(c)** T5 tunnel gates is given. These are hysteresis curves: we first sweep the gate voltage in one direction (0.0 V → -0.5 V, black curve), and then back in the other (-0.5 V → 0.0 V, red curve). This is significant, as the similarity between the two curves is an indicator of the stability of our device. An important thing to keep in mind is that if the refrigerator is thermally cycled, pinch-off traces change as well, thus these curves, although for the same gates on the same device, might differ from the ones given in Appendix C.1.

To do so, we can measure the current through the system, and plot so-called *pinch-off curves* for each of the gates, an example of which for one of the devices is pictured in Fig. 4.3. While these curves provide a good estimate of the *pinch-off voltage*[5], they mostly serve only as a rough indicator of the ranges of voltages necessary to provide weak tunnel coupling between the two dots. To this end, we usually perform a more "zoomed-in" RF measurement monitoring the reflected signal, as a function of the tunnel gate voltage and dot's side plunger gate voltage, trying to determine what ranges give us the brightest (in this case) 2e periodic response. For the first (second) device in our experiment, we applied electric voltage of of $T3 = T5 - 2\ V$ ($T2 = T4 = -1.3\ V$), while setting the middle barrier $T4 = -0.385\ V$ ($T3 = -0.4\ V$). For the DC and RF pinch-off scans of our device, see Appendix C.1.

Returning to the theory chapter, a standard method of characterising the SC-QD double dot, is by measuring the DC current (or RF signal) by sweeping the chemical potential of the charge islands using their plunger gates, together with the bias voltage V_{bias}. This way, we obtain Coulomb diamonds - Coulomb blockade regions of stable charge state configuration, whose dimensions are directly determined by the characteristic energies of the system (as illustrated in Fig. 2.2). To focus only on the SC-QD double-dot system, the gates *not* defining the double dot are 'opened' not to affect the system. This is achieved by simply setting them to zero voltage, thus effectively extending the leads. It should be mentioned at this point, that the second sample showed no conductance between the lead and the drain[6], making Coulomb

---

[5] The voltage needed to completely suppress the current across the barrier, make the island *floating*.

[6] There still was conductance between individual dots, as well as functional gates allowing for QD-SC system to be defined in the floating regime, thus making the experiment possible. The likely reason for that was a disconnect at the contacts, or one of the bonds failed.

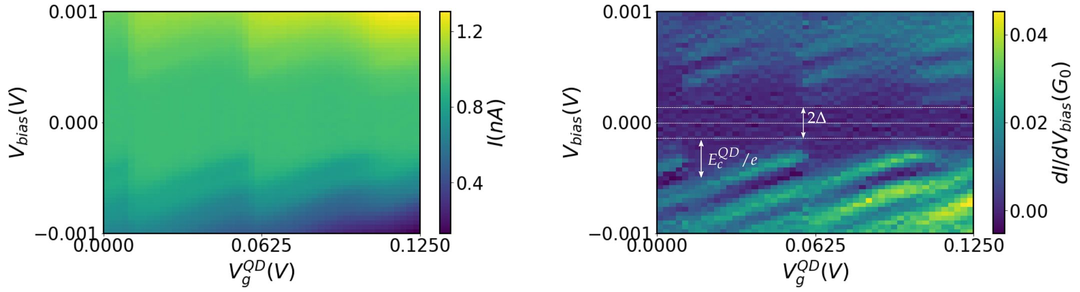

FIGURE 4.4: Coulomb diamonds for the normal QD. Left panel shows current as a function of gate voltage and bias, while the right figure shows conductance (numerical derivative of the current, with respect to the bias voltage) in units of *conductance quantum*. In a similar way, we can determine the charging energy of the SC (See Appendix C.2).

diamond DC measurement impossible. In that case, a CSD of the double dot system could still be measured through RF sensing, although no claims about any precise value of energies of the system could be made without the knowledge of the lever arm.

A Coulomb diamonds DC current scan of the first device is shown in Appendix C.2. The most striking feature to notice in the scan is that the diamonds overlap due to superconductive leads. The Coulomb blockade diamonds, centred around zero bias spread out due to the blockade induced by the superconducting gap in the SC. This enforces another tunnelling restriction on the energy the electrons must obey. At the same time, this implies that the value of $\widetilde{\Delta}$ can be read off the plot as the width of the blockaded region. By measuring the height of the gap, as well as the dimensions of the triangles on each side of it, the charging energy of the dot, as well as its lever arm, can be determined. For the first sample, the values estimated from the Coulomb diamonds are $E_c^{QD} \approx 350\ \mu eV, E_c^{SC} \approx 135\ \mu eV, \widetilde{\Delta} \approx 125\ \mu eV$ and lever arms of $\alpha^{QD} \approx 0.8\%, \alpha^{SC} \approx 1.1\%$ for the normal QD and SC island, respectively.

To draw the correspondence between the resonant frequencies of the resonators and plunger gates, we can perform a full sweep of the probe frequency, noting resonances as dips in the amplitude of the spectrum. Results of such a scan for the second device are shown in Fig. 4.5, while the zoomed-in scans are given in Appendix C.3.

Both VNA and OPX can record the full complex transmission, so the resonator response can be given in terms of the magnitude and phase, which can be translated into the in-phase (I) and quadrature (Q) components. This way, measuring many RF responses for a particular energy configuration of the system, the two components from the complex signal can be extracted and represented in a 2-dimensional IQ histogram. This way, a single peak in the histogram indicates a single frequency response, while any splitting behaviour of the histogram indicates a two-level response. Thus, this provides a handy and robust tool for the analysis. This will be further illustrated in Section 4.4.

Lastly, we want to tune the power of the resonator to a suitable value. The optimal SNR is a subject of balance between two competing factors. Namely, increasing the power increases the signal relative to the noise, but at the same time drives more

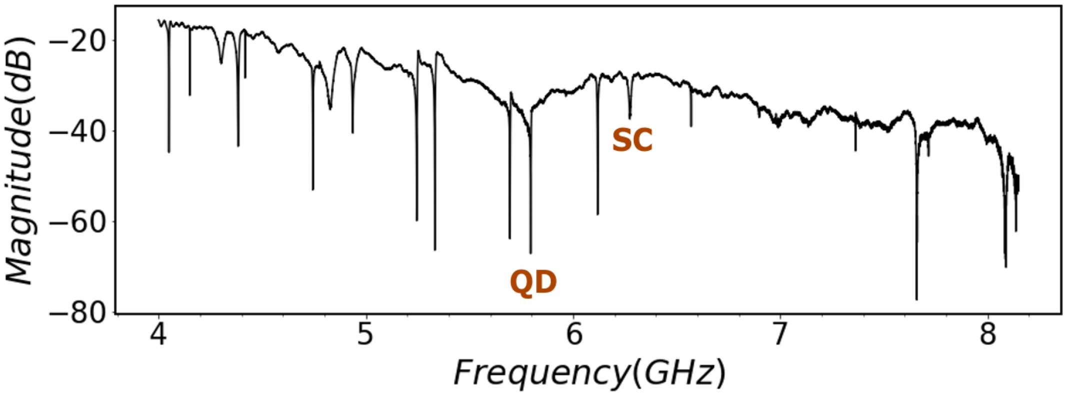

FIGURE 4.5: Resonator response for the second device. The responses identified to correspond to the normal dot and the SC dot plunger gates are indicated on the plot. Using a fitting algorithm, their frequency values of 5.79579 GHz and 6.28044 GHz, respectively, are extracted. Other dips correspond to the plunger gates of other dots present on the chip. As there are two devices mounted on the resonator chip simultaneously (see Fig. 3.2) half the peaks correspond to either of the two devices[7].

excitations in the double dot, which reduces the frequency shift. An initial power scan of the first device is given in Appendix C.4, but a more detailed treatment is described in Section 4.4.1.

4.4 Experimental Data

The experimental section consists of five main parts. First, temporal scans and their heavy analysis are presented for systems in which we vary the tunnel gate between the two dots (1), for systems where we intentionally try to induce quasiparticle poisoning events, either by increasing the RF power (2) or increasing the operating temperature of the refrigerator (3). Additionally, we report an observation of histogram splitting behaviour on resonances in certain scans (4), and finally discuss the results, and list possible theoretical and practical limitations of the experiment (5). Measurements reported in (1), (2), and (4) were performed on the first device, while the temperature scans on the other one[8].

At this point, the refrigerator is cooled down to the base temperature of 15 mK, the gates of the quintuple dot device are appropriately pinched, forming a double dot with an intermediate interdot coupling displaying an even-odd CSD pattern, with resonators of different characteristic frequencies capacitively coupled to each of the two dots, allowing for reflectometry readout. In the experiment, the chemical potential of the SC is held constant throughout the measurement. At the same time, the voltage on the plunger gates of the normal quantum dot is swept, in line with the horizontal line-cut through a CSD for the double dot system, as the one indicated by

---

[7] Note: of the two devices on the chip, measurements presented in this thesis were performed only on one.

[8] There is no particular reason for that division other than the availability of devices at the time of measurement.

a purple line in Fig. 4.2b. A suitable voltage on the SC dot is set, such that the system is tuned into a regime with even-odd spacings and displaying little charge jumps[9]. These values, along with the value of the interdot gates, were varied through the experiment according to conditions listed above.

4.4.1 Power Scans

The idea is relatively straightforward; as noted in Fig. 4.2a, a sample without proper shielding was subjected to large amounts of high-frequency environmental radiation, causing a steady-state presence of quasiparticles on the island. Similarly, by intentionally radiating the system with high-power RF signal we hope to induce Cooper-pair breaking and get a few-quasiparticle population on the island, which could manifest as a third and fourth peak within the Coulomb blockade. We further investigate if that only happens when we are radiating the SC's gate, or if there is some cross-coupling interaction when applying the power on the neighbouring dot. In order to conduct the experiment, we slightly reconfigure the setup by unplugging the VNA and plugging an RF source, so that we can input a constant RF signal through one of the resonators coupled to either the SC's or the normal QD's gates, while independently measuring the other one using OPX.

We scan the QD gate voltage range between $V_g^{QD} = -1.9\ V$ and $V_g^{QD} = -1.4\ V$, covering about 4 transitions (producing roughly two pairs of parallel lines). We find that $V_g^{SC} = -1.35\ V$ yields a good regime, which is a value we use throughout the entire power dependence investigation. At each point along the V_g^{QD}, 1.000 responses are measured, each of 1 μs in duration. An example of one of such temporal power scan is given in Fig. 4.6a, with the averages of all power scans, show in Fig. 4.6b.

From the plots, we can see that increasing power above -110 dBm diminishes the response, as expected from the preliminary power dependence scans. The curves are intentionally offset (1.3 rad) along the vertical axis for clarity, while the offset along the horizontal axis (most notable when comparing the scans of -130 dBm and -120 dBm) could be explained by a charge jump that occurred in-between the two measurements. The expected power dependence of the imparted phase shift is observed, with a gradual decrease in the height of the peaks towards the upper and bottom limits of applied power. However, concerning the quasiparticle poisoning, we cannot claim much from this plot - in particular, after averaging no third or fourth peak can be visible, so the further subsequent analysis is required.

By plotting a histogram of the 1.000 I/Q values at each voltage, we can investigate the response more precisely. However, as it turns out, having only 1.000 points yields very scattered histograms, making it extremely challenging to reach any conclusions about the general shape of the distribution. Assuming Gaussian distribution of the histograms, we can fit each of them using a double 2-dimensional

---

[9] A sudden and random change in the electrostatic surrounding of the island (for example an electron in the gate oxide jumping closer to the island), which slightly offsets the CSD.

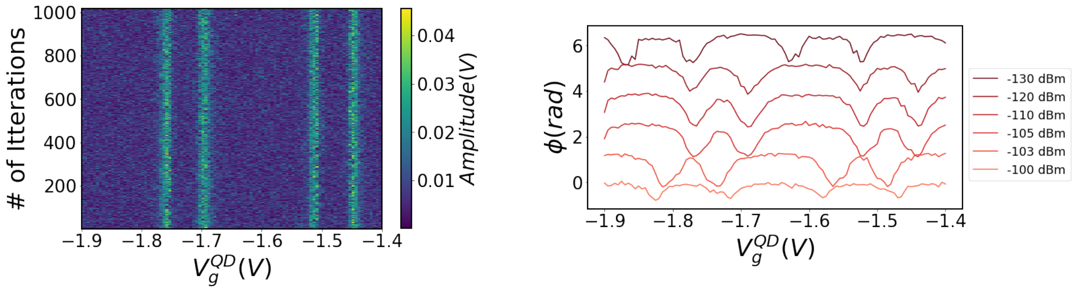

(a)

(b)

FIGURE 4.6: **(a)** An temporal scan corresponding to resonator probe power of -120 dBm at the sample level. Each point along the V_g^{QD} in range of 0.5 V was measured 1000 times, represented in the plot as the vertical axis. Even-odd spacings are still visible. **(b)** The effect of different powers is summarised, different curves are offset for clarity. All of the responses plotted in figure were obtained by applying the RF power to the resonator of the SC dot. There was no significant change when applying the RF power to either of the neighbouring dots.

Gaussian curve. We can compare the distributions characteristic of Coulomb blockades with those around the voltages where the third and fourth peak are expected to show on the diagram. Their positions within the even regime is $(S_{even} - S_{odd})/2$ distant from each of the two lines bounding the wide spacing, with S_{even} (S_{odd}) the even (odd) spacing in the diagram (as illustrated in Fig. 4.7 and explained in Appenedix B). Examples of histograms for an intermediate power of $P = -110\ dBm$, at resonance, the expected QPP regimes and within Coulomb blockade are illustrated in Fig. 4.7, with additional figures for low and high power limits presented in the Appendix C.4. The remainder of the analysis in this thesis was mostly done in the same or very similar manner.

4.4.2 The effects of tunnel gate T4

Next, we investigate the effects of varying the interdot gate voltage of the system. Following an approach analogous to the one presented above, we conduct the experiment, where we construct a 4-dimensional data set: V_g^{QD} vs *iterations* vs *resonator response* vs *T4*. Here we investigate if any notable effects arise when we vary the voltage on the tunnel gate between the two dots. As the tunnel gates are directly related to tunnelling amplitudes, it could be expected that decreasing the tunnel barrier increases the probability of the quasiparticles tunnelling between the island and the dot. We sweep over the gate voltage range between $-1.9\ V$ and $1.4\ V$ in 201 increments, tunnel gate voltage T4 range between $-0.1\ V$ and $-0.2\ V$ in 101 steps, while at each combination of the two, recording 10.000 1 μs pulses measuring the amplitude and phase (or I and Q) values. Following the histogram-analysis presented in the section above, the aim is to investigate if any of the histograms distributions show splitting, elongation or any behaviour indicating a resonator response alternating between different values. To summarise the results, in short, varying T4 seems

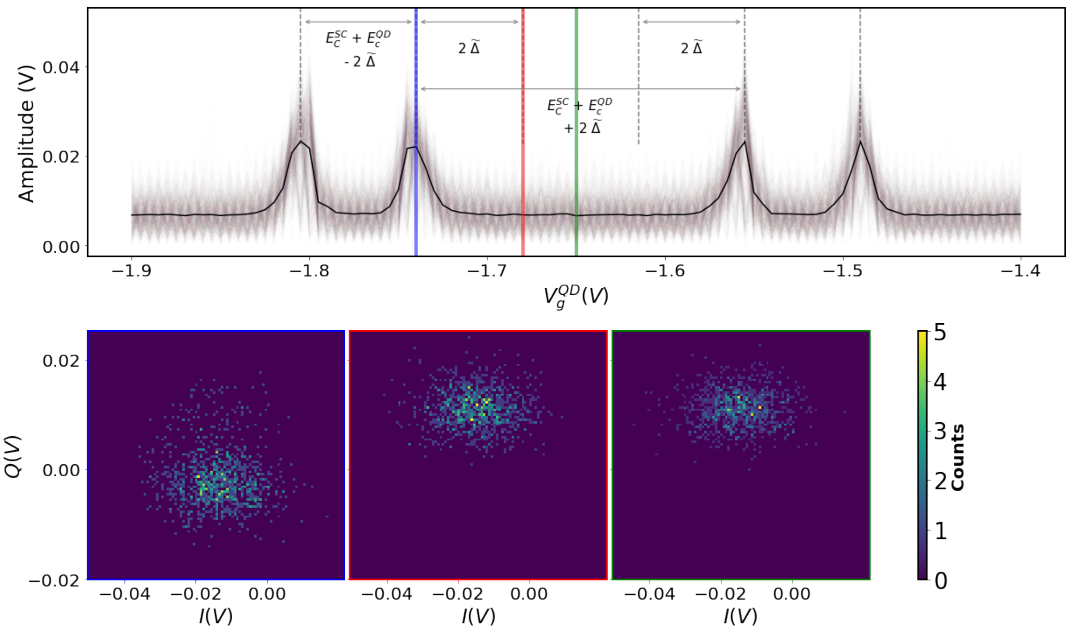

FIGURE 4.7: The power scans analysed using histograms. The top plot shows the relation between the gate voltage and the measured amplitude of the signal. The white line shows an averaged response, clearly showing two pairs of even and odd regimes. Using a peak finding algorithm, we can determine the positions of resonances, as well as calculate the expected positions of QPP peaks. We compare average histograms of Coulomb resonance (bottom left, blue), along the line where we expect the shadow peaks (bottom middle, red) and deep within Coulomb blockade (bottom right, green). The resonator response changes when on resonance due to electron tunnelling, while no distinguishable difference can be determined between the two other responses. The histogram of the resonant case shows a splitting of the histogram distribution, rather than simply shifting. We discuss this in more detail in Section 4.4.3.

to have no noticeable effect on the telegraph plot, once the tunnel gate is tuned in a suitable regime (as in Figs. C.1 and C.2). Similar to the measurements above, there is a significant on-resonance dispersive shift, but histograms from within the Coulomb blockade show no distinct pattern.

Having more points in the IQ histogram plane, the power dependence analysis can be improved by more carefully scrutinising each of the histograms of interest. In particular, the histograms of potential shadow peaks are compared with the averaged response from all scans within the Coulomb blockade. In this way, effective background filtering is achieved. In Appendix C.5, a concept of Gaussian division of the two plots is introduced, where we show how tiny shifts manifest as distinct coronae. However, even after such investigation, no particular response could be detected for off-resonant cases. However, a particularly interesting response was noted at some resonances of some values of T4.

4.4.3 Two Level Fluctuator

In some cases, a *splitting* behaviour rather than *shifting* is detected on Coulomb resonances. An example of such splitting for the tunnel gate $T4 = -0.36\ V$ is illustrated in Fig. 4.8 (some splitting behaviour can also be seen in Fig. 4.7). In general, we expect to record a signal characteristically different from the one within Coulomb blockade, which shows as a histogram distribution with a shifted peak. Using dispersive gate sensing (DGS), a single shot readout with an SNR of 2 for an integration time of 1μs has been previously reported, enabling differentiation between the Coulomb blockade and resonance [48]. In the context of measurement-based quantum computation, such as Majorana qubits, DGS has been proposed in some architectures as a viable way of high-fidelity and fast readout. Such resonant splitting as repeatedly observed in some regimes might prove to be a limitation to these architectures, so it requires further analysis. At the same time, this investigation provides a set of useful tools, in analysing a time-resolved telegraph signal of the resonator response, such as we might observe in the case of quasiparticle poisoning.

First, the split histogram is fitted using a 2-dimensional double Gaussian function, as in Fig. 4.8 below. Using the obtained peaks, as well as other Gaussian parameters, we can (first rotate, then) divide the histogram into three parts, characterising which section the resonator response falls into, with the middle section the "undefined" zone. An example of the histogram of responses in Fig. 4.8 is given in Fig. 4.9a. Finally, as these responses were measured in time, we can plot the telegraph signal (Fig. 4.9b), and infer counts of (confidently characterised) resonator response for each of the two histogram peaks, and average and maximum times of the system giving one or the other resonator response. By measuring the time dynamics of the two responses, we can gain knowledge about the time dynamics of the system itself.

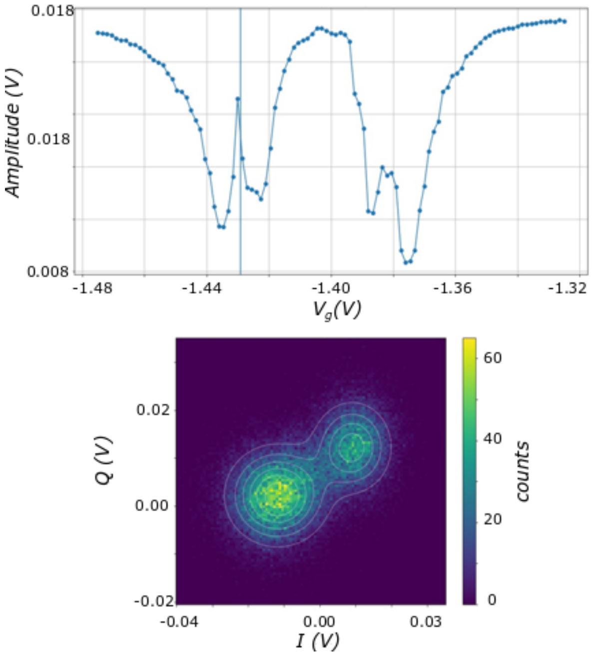

FIGURE 4.8: Splitting on resonances. In some cases, a splitting of the IQ histogram was observed on Coulomb resonance. The upper plot shows an averaged scan, while the bottom one shows the histogram of all resonator responses measured at the particular value of V_g^{QD} (vertical line on the upper plot).

Physically, the two different responses indicate the presence of two different quantum states. Although this could be explained by excess quasiparticles on the island, where a QP poisoning event is effectively causing the system to be in a blockade regime, we rule this option out, as in that case, we would also expect to see some shadow peaks within the Coulomb blockade. The most probable explanation for that, however, is that somewhere in the dielectric, some form of a two-level fluctuator is coupling to the system, causing the two-level response in the resonator response. This claim is further supported by the fact that at different tunings, the distribution splitting seems to be random.

4.4.4 Temperature Dependence Scans

Finally, the last mechanism with which we try to induce Cooper pair breaking and subsequent poisoning events is by raising electron temperature. As introduced in Section 2.2, superconductivity is achieved when the temperature of some materials is sufficiently lowered below a particular, material dependent critical temperature T_C, which is for aluminium at 1.2 K [63]. Contrary to the prediction implied in Eq. 2.14, that at $T = 0$, $f(E_\mathbf{k})$ goes to zero for all momenta $\mathbf{k}$, experiments show, that at low temperatures quasiparticle density saturates to a constant value [19, 21]. As we expect the rate of QP tunnelling to depend on the number of excited quasiparticle

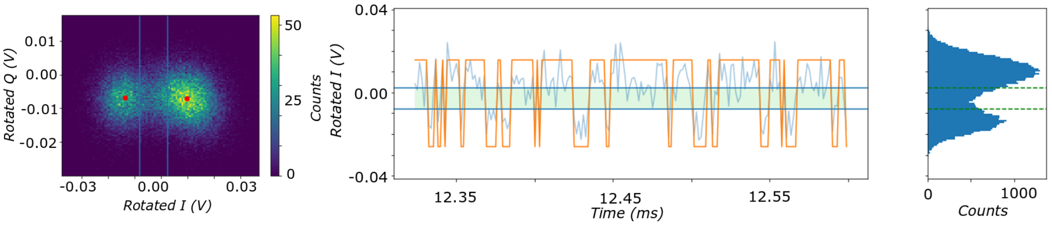

(a)

(b)

FIGURE 4.9: By analysing the telegraph signal, we can determine the average occupancy of each of the two states, giving two responses in the IQ plane. **(a)** shows a rotated histogram after the two distributions have been identified, and the histogram has been rotated. We define a middle section, from which the resonator responses cannot be reliably identified. **(b)** An insert of the telegraph signal, showing the alternation between the two states. Points in the middle do not affect the switching, and are assigned to the distribution from which the last response came. This way, we obtain the *upper* limit time values. For this particular scan, the average dwell times of the left and right distribution are 5.00 μs and 9.40 μs, respectively.

states on the SC island N_S, it is worth relating the temperature to the actual number of quasiparticles on the island [64]

$$N_S = 2D(E_F)V \int_{\Delta}^{\infty} dE \frac{E}{\sqrt{E^2 - \Delta^2}} f_E \tag{4.1}$$

$$\approx \sqrt{2\pi} D(E_F) V \sqrt{\Delta k_B T_S} e^{-\Delta/k_B T_S}. \tag{4.2}$$

Using the literature value for the normal-state density of states at Fermi energy in aluminium $D(E_F) = 1.45 \times 10^{47} J^{-1} m^{-3}$ [59] and estimating the dimensions of our SC island approximately $V = 1\mu m \times 70nm \times 7nm$ ($L = 1.9\ \mu m$ for the second device), we can roughly estimate the expected number of excess charges as a function of the temperature of our bath. An important thing to note here is that this equation describes systems with a hard superconducting gap, which is not the case in superconductor-semiconductor systems. This can still serve as a top-limit estimate at what temperatures we might expect to be in a regime of few quasiparticles on the island, and what temperature resolution we would require in order to separate between 'few' and 'many' QP regimes on the island. For a typical value of the superconducting gap between 100 and 200 μeV, the interplay between the average number of QPs on the island and the temperature of the bath is illustrated in Fig. 4.10.

The estimates from Fig. 4.10 give us an indication of the ranges of temperatures that coincide with a few QPs on the island and give a rough indication of what resolution of temperature would be required to observe that transition. Not enough QPs would result in no signal (as reported in sections above), while too many QP's on the island would turn the signal 1e periodic. Similar results were previously already reported in [62]. Luckily, some control over the temperatures in the fridge can be implemented. In particular, for this experiment, the response of the resonator as a function of both gate voltage and the temperature is measured 30.000 times, with 1 μs pulses, as before. The full parameter space over which the device was

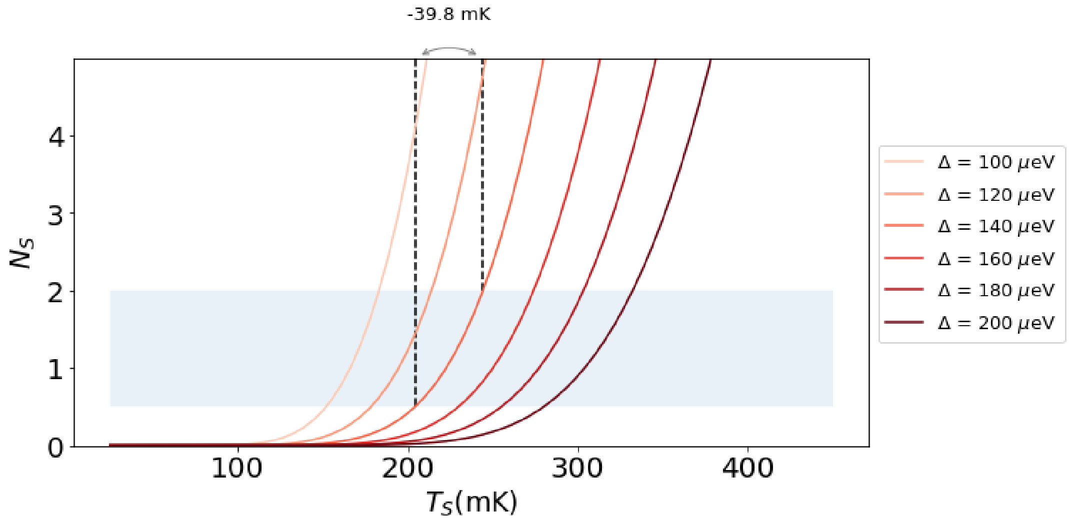

FIGURE 4.10: The quasiparticle number as a function of the temperature of the sample. As we do not precisely know the value of our superconducting gap, this plot serves mostly as an upper limit estimate of the temperature regime, and resolution we would require to manipulate the average excess QP number on the island to be between 0.5 and 2. For our system, these numbers are realistic, motivating us to investigate this further.

characterised is summarised in Table 4.1.

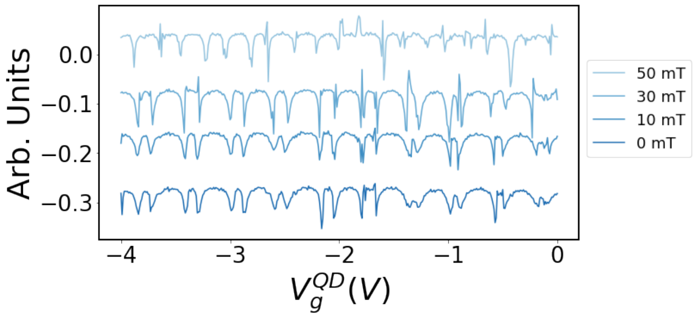

FIGURE 4.11: Magnetic field dependence, vertical axis offset for clarity. As the magnetic field is increased, 2e to 1e transition is noticable, in line with superconductivity in our sample.

For the investigation of the temperature dependence, only the second sample was used. To establish the presence of the superconducting gap and thus confirm the origin of 2e periodicity in the CSD in the floating regime, the sample was first swept through a magnetic field. As superconductivity at large magnetic fields is effectively destroyed, we should be able to notice a 2e to 1e transition in the spectrum (as observed in Fig. 4.11). Additionally, from the zero-field scan, even-odd spacings can be determined, from which the charging energies (corrected with an unknown lever arm α, presumably in 0-1 %) can be obtained. We measure the average even and odd spacings to be $S_e = 0.2985\ V, S_o = 0.11613\ V$, respectively, yielding $\alpha\widetilde{\Delta} = 0.0457\ eV$.

We follow the same analysis of this data-set, as described in sections above. After investigating initial average scans (presented for temperatures near the 2e to 1e transitions in Fig. 4.12) for subtle third and fourth peaks (to no avail), histograms for different values are investigated using the method presented above and in Appendix C.5. As expected, by increasing the temperature, initially 2e diagram transitions into

T3	T2 = T4	OPX Power	$\omega_0(QD)$	V_g^{QD} range	T range
-0.4 V	-1.3 V	-39.81 dBm	5.79548 GHz	-4 V → -1 V -8 V → -5 V	15 mk → 240 mK

TABLE 4.1: Parameter space for the temperature sweeps. Operating at increasing temperatures, re-tuning of the voltage range was required to ensure large enough SNR. In both cases, the system was scanned in increments of 0.005 V. The operational temperatures of the refrigerator were 15 mK (base temperature), 100 mK, and between 150 mK and 240 mK, in increments of 10 mK. Initial VNA scans indicated 1e periodicity at 240 mK, confirming the prediction from Fig. 4.10 for a gap on the order of hundred μeV.

1e periodic V_g^{QD} dependence on the reflected signal. Although the transition is gradual, "by-eye" we estimate that the transition happens between 180 mK and 190 mK. As before, resonant configurations are observed as a shift in IQ histograms, while no such pattern can be detected for configurations allowing for QP tunnelling events. One of the bigger limiting factors in the analysis is the fact that due to small value of $\widetilde{\Delta}$, even and odd regime spacings S_{even}, S_{odd} are nearly the same, which places the two shadow peaks at the foothills of the degeneracy peaks. As the last point, it is worth mentioning that we did not observe any two-level fluctuators on resonances in either of the temperature scans.

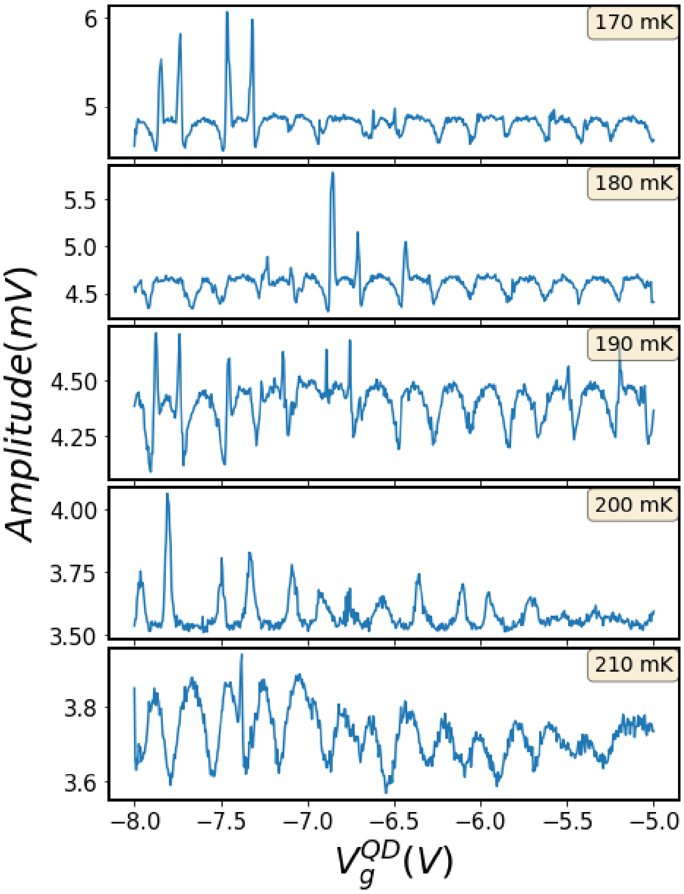

FIGURE 4.12: Averaged scans for different temperatures between 170 mK - 210 mK, where the 2e to 1e transitions gradually occurs.

4.5 Discussion

So, where are all the quasiparticles? Or better yet, *why aren't we seeing any?* In this section, we explore and evaluate the two limitations that prevent quasiparticle tunnelling from being seen. First, we evaluate the methods used in this experiment, and secondly, we investigate the physics of quasiparticle excitation relaxation and poisoning rates.

It is useful to first discuss the limitations of our method. The time resolution of the experiment is limited by a couple of factors. First, the length of the pulse integration time is 1.000 μs, with about 400 ns of wait time in-between pulses. This can roughly serve as a lower bound for the time resolution. The upper bound is somewhat related to the length of the entire measurement along a single voltage, which in our experiment ranges between 1 and 30 ms (between 1000 and 30 000 iterations). This means that the processes with rates that fall within this range can be measured using the setup. Clearly, a process with rates much higher or much lower than this resolution can not be resolved. We discuss the interplay of these rates a bit more into detail later on.

Another methodological limitation comes from determining the energy values of the system. Although for the analysis, relative energy values will do the trick, in order to draw any conclusions and to calculate expected rates at various conditions, these values can prove to be very useful. However, as the second device was slightly damaged, we were not able to precisely determine the values of the charging energies, which made temperature dependence calculation slightly less precise.

In the experiment, we need to acknowledge three main rates, determining the dynamics of the system: tunnelling rates between the island and the dots Γ_t, the quasiparticle poisoning rates (excitations from within the condensate) Γ_{exc}, and quasiparticle relaxation rates Γ_{rel}. These rates are schematically illustrated in Fig. 4.13. The interplay of these rates should determine the number of quasiparticles present on the island, and the amount of QP that we can detect using DGS. Do note that these two numbers are not necessarily the same, which might explain the lack of the detected signal around the shadow peak locations. In particular, either the recombination rate of QP is much larger than the tunnelling rate (so the QPs will preferentially want to stay on the island), or the excitation rate is much lower than the recombination rate (so the QPs are very rarely generated, and when they are, they recombine quickly).

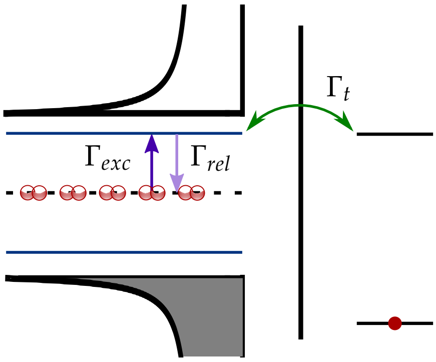

FIGURE 4.13: The rates present in the system, assuming any external no external sources of quasiparticle generation is negligible compared to the rates from within the island. By investigating these rates, we can better understand the dynamics of the system.

Let's first take a look at the relationship between the recombination and tunnelling rates. Importantly to note, DGS does not measure a single electron tunnelling events. Rather, it indicates a degeneracy of two energy levels, when an electron present on one can tunnel back and forth between the two dots thousands of times, with rates on the order of GHz [48]. If the rates of recombination of quasiparticles on the SC island are much larger than the rates of tunnelling between the dots, the electron might recombine back in the condensate much too often, leaving behind no characteristic footprint in the resonator response as compared to the Coulomb blockade.

Detailed Balance condition rates

An important question, that has to be addressed in any telegraph measurement of physical systems, is what are the expected rates of the processes we attempt to measure. In the case of this experiment, rates we are in particular interested in are the excitation and relaxation rates of quasiparticles. To do so, we investigate the balanced condition rates. The idea is that in any kinetic system in equilibrium, the system's elementary processes should also be in equilibrium with their reverse process. For the systems under investigation here, we need to consider two states, the ground state, where all the electrons are neatly paired up in Cooper pairs, and there is no excess of quasiparticles on the island (a non-poisoned state), and the excited state, where we have some finite unpaired electrons on the island (poisoned state). The energy difference between the two states depends on the energy gap of the superconductor - the minimal energy that is needed in order to break a Cooper pair, $2\widetilde{\Delta}$. The transition rates between the two states can be visualised as in Fig. 4.13, where Γ_{exc} is the rate of exciting quasiparticles, and Γ_{rel} the rate of their relaxations. These two rates are related to one another through

$$\Gamma_{exc} = e^{-\Delta E/k_B T}\Gamma_{rel} \tag{4.3}$$

where ΔE is the energy cost of the transition, which in our case equals $2\widetilde{\Delta}$. To avoid explicitly predicting the two rates, further analysis can be done by simply investigating their ratio, which for typical value of the the energy difference $\widetilde{\Delta} = 150\mu eV$ and quasiparticle temperatures up to 1 K[10]

$$\frac{\Gamma_{exc}}{\Gamma_{rel}} = e^{-\Delta E/k_B T} \approx 0.06 \quad \text{(at 1 K)} \tag{4.4}$$

$$\approx 9 \times 10^{-7}. \quad \text{(at 200 mK)} \tag{4.5}$$

This yields the rate of excitations many orders of magnitude below the number for the rates of relaxations. At the same time, for very low QP concentrations, the relaxation rate can be suppressed by virtue of the fact that it takes a while for two quasiparticles to find each other and recombine.

---

[10] Reports from [20] cite quasiparticle temperature to be slightly larger than the electron temperature.

Chapter 5

Conclusion and Future Directions

In this thesis, we have briefly introduced the working theory of (superconducting) quantum dots, elucidated the principles of dispersive gate sensing, and attempted to scrutinise a paradoxically known yet unexplored problem of quasiparticle poisoning (QPP) in superconductor-semiconductor hybrid double dot devices. Although many previous experiments have been done investigating the rates related to the poisoning processes, most of the available research data describe the dynamics in pure superconducting devices or investigate the systems coupled to galvanic leads, which are in itself a significant source of quasiparticles. In this work, we focus on isolated superconducting islands embedded within a hybrid device, like the ones proposed to host Majoranas.

To that extent, we have used a technique of dispersive gate sensing (DGS) and designed an experiment in which we investigate the processes arising when excess quasiparticles are present on the island. Using reflectometry for the purposes of DGS, we were able to carry out the experiment in a so-called floating regime, where using voltage-controlled tunnel gates, we were able to suppress external tunnelling events from the nearby leads. This enabled us to focus solely on the internal poisoning processes of the superconductor, which were previously unexplored. Using time-resolved spectroscopy, we recorded charge-tunnelling dependent resonator responses with a microsecond integration time. In principle, for a process occurring at rates that are slower than the measurement frequency, this technique can be used to convert a relatively faint difference between two states (for example a poisoned and an unpoisoned state), into a much clearer signal of the gate being either on Coulomb resonance versus on Coulomb blockade.

As no clear signal could be visible at the base temperature at normal operational conditions, we attempted to intentionally induce quasiparticle poisoning by irradiating the sample with radio-frequency (RF) power, and by increasing the temperature - both known factors with an effect of increasing the average number of quasiparticles above the SC gap in superconductors. However, no QP tunnelling processes could be observed. A possible answer to this observation could be provided by the principle of detailed balance. It predicts that in thermal equilibrium at temperatures used in cryogenic refrigerators, Cooper pair breaking rate falls multiple orders of magnitude short of the recombination rates. Alternatively, the models for superconducting systems we used to predict thermal effects might wrongly estimate the quasiparticle density in hybrid devices and do not account for how the presence of the Majorana modes itself changes n_p. Lastly, as the signal-to-noise ratio becomes increasingly smaller at higher temperatures, as well as higher powers, quasiparticle poisoning events might impart a minuscule dispersive shift, which hides within the noise level of the device. For a more precise value, a quasiparticle number fluctuation using a master equation formalism could be investigated, similar to the one presented in [65].

Additionally, we have shown how a long telegraph measurement can make visible processes which are not necessarily evident from an averaged measurement. This was further illustrated with the two-level fluctuator example, whereby characterising a telegraph signal of two distinct histogram peaks in the I/Q plane, we were able to determine average dwell times, and characteristic lifetimes of each state. This approach is also well suited for quasiparticle poisoning data analysis, where two different responses from the resonator would indicate either a poisoned or an unpoisoned state.

An important thing to note is that not observing a shift, does not necessarily imply that the island is not poisoned. DGS does not measure a single electron tunnelling events, but rather indicates a degeneracy of two levels, where an electron can tunnel back and forth thousands of times, with rates on the order of GHz. If the rates of recombination of quasiparticles on the SC island are much larger than the rates of tunnelling between the dots, the electron might recombine back in the condensate much too often, leaving behind no characteristic footprint in the resonator response.

To that end, an improvement to the proposed experiment could be made, where these rates are increased in one way. By adding a second quantum dot to the double dot system, we could design a sort of "vacuum cleaner" for the quasiparticles on the island. By tuning the two dots in resonance with one another, but slightly below the resonance with respect to the gap of the SC island, we could measure the tunnelling events between the two dots. If initially, the two energy dots are empty, the only source of electrons would be from above the gap of the superconducting island. In this way, further insight into the dynamics of quasiparticles on the island could be made.

Finally, a fair question that still needs to be addressed in relation to the outlook of the experiment is whether the setup proposed in the experiment, where a double dot system is completely decoupled from any leads, can be used in a context of qubits, more precisely, Majorana qubits. Based on recent proposals for scalable designs allowing for QPP-protected topological quantum computing [13, 14], a device predicted to host a topological qubit can (in theory) be operated entirely within the Coulomb blockade relative to the leads. It stands to reason that the qubit could, therefore, be realised and measured in a floating regime using DGS. Particularly, if the poisoning times are significantly shorter in floating regimes, this could probe the way towards even more protected qubit schemes.

Appendix A

Toy Model for Excited State Driving

A.1 Hamiltonian in the Rotating Frame

The Hamiltonian for a double dot with finite tunnel splitting is given by

$$H/\hbar = \frac{\tau}{2}\sigma_z + \frac{\epsilon}{2}\sigma_x. \tag{A.1}$$

where $\tau = \frac{2t_c}{\hbar}$, with $2t_c$ being the full splitting of the anti-crossing at charge degeneracy, and σ_i the Pauli matrices given by

$$\sigma_x = \begin{pmatrix} 0 & 1 \\ 1 & 0 \end{pmatrix} \quad \sigma_y = \begin{pmatrix} 0 & -i \\ i & 0 \end{pmatrix} \quad \sigma_z = \begin{pmatrix} 1 & 0 \\ 0 & -1 \end{pmatrix}, \tag{A.2}$$

with simple commutation relations given by

$$[\sigma_i, \sigma_j] = 2\epsilon_{ijk}\sigma_k,$$

with ϵ_{ijk} the Levi-Civita symbol. Modulation around degeneracy with frequency ω implies

$$\begin{aligned}\epsilon(t) = \epsilon_0 \cos(\omega t) =& \frac{E_C C_g V_{rf}}{e\hbar}\cos(\omega t) \\ =& \frac{e\alpha V_{rf}}{\hbar}\cos(\omega t),\end{aligned} \tag{A.3}$$

with V_{rf} the maximum amplitude of the RF gate voltage around the degeneracy point. In the last part we use the double dot electrostatic energy given by [33]. By defining the unitary operator U as $U = \exp\left(i\frac{1}{2}\omega t\sigma_z\right)$,, the Hamiltonian transforms according to:

$$H/\hbar \rightarrow U(H/\hbar)U^\dagger + i\dot{U}U^\dagger := \tilde{H}/\hbar, \tag{A.4}$$

with daggers denoting complex conjugates, and the dot above U time derivative. The second part of this equation, $i\dot{U}U^{\dagger}$, can be evaluated relatively straightforwardly:

$$\begin{aligned} i\dot{U}U^{\dagger} =& i^2\frac{1}{2}\omega\sigma_z \exp\left(i\frac{1}{2}\omega t\sigma_z\right)\exp\left(-i\frac{1}{2}\omega t\sigma_z\right) = \\ =& -\frac{1}{2}\omega\sigma_z. \end{aligned} \tag{A.5}$$

The first part requires a little more effort. The idea is to commute the $U^{\dagger}$ operator through the Hamiltonian, where on the other side it will cancel out with U operator. As the operators of the Hamiltonian will not necessarily commute with the operators of the rotation operator U, this will result in extra terms.

$$\begin{aligned} U(H/\hbar)U^{\dagger} =& e^{i\frac{1}{2}\omega t\sigma_z}\left(\frac{\tau}{2}\sigma_z + \frac{\epsilon}{2}\sigma_x\right)e^{-i\frac{1}{2}\omega t\sigma_z} \\ =& \underbrace{e^{i\frac{1}{2}\omega t\sigma_z}\left(\frac{\tau}{2}\sigma_z\right)e^{-i\frac{1}{2}\omega t\sigma_z}}_{=\frac{\tau}{2}\sigma_z,\text{ as }\sigma_z\text{ and }\sigma_z\text{ commute}} + e^{i\frac{1}{2}\omega t\sigma_z}\left(\frac{\epsilon}{2}\sigma_x\right)e^{-i\frac{1}{2}\omega t\sigma_z} \\ =& \frac{\tau}{2}\sigma_z + e^{i\frac{1}{2}\omega t\sigma_z}\left(\frac{\epsilon}{2}\sigma_x\right)e^{-i\frac{1}{2}\omega t\sigma_z} \\ =& \frac{\tau}{2}\sigma_z + \left(Icos(\frac{1}{2}\omega t) + i\sigma_z sin(\frac{1}{2}\omega t\right)\left(\frac{\epsilon}{2}\sigma_x\right)\left(Icos(\frac{1}{2}\omega t) - i\sigma_z sin(\frac{1}{2}\omega t\right) \\ =& \frac{\tau}{2}\sigma_z + \left(Icos(\frac{1}{2}\omega t) + i\sigma_z sin(\frac{1}{2}\omega t\right)\left(Icos(\frac{1}{2}\omega t)\frac{\epsilon}{2}\sigma_x - i\frac{\epsilon}{2}sin(\frac{1}{2}\omega t)\sigma_x\sigma_z\right). \end{aligned}$$

where the exponent was expanded according to the Euler's identity

$$e^{i\frac{1}{2}\omega t\sigma_z} = Icos(\frac{1}{2}\omega t) + i\sigma_z sin(\frac{1}{2}\omega t).$$

Here, the commutation of σ_x and σ_z is not straightforward. We need to consider the commutation relation between the two Pauli matrices, $[\sigma_i, \sigma_j] = 2\epsilon_{ijk}\sigma_k$, with ϵ_{ijk} being the Levi-Civita symbol. For the case of σ_x and σ_z this expression yields $[\sigma_x, \sigma_z] = \sigma_x\sigma_z - \sigma_z\sigma_x = 2i(-1)\sigma_y$, which means that we can replace the $\sigma_x\sigma_z$ in the expression above with $\sigma_z\sigma_x - 2i\sigma_y$. Remember, the motivation behind this is to commute the Hamiltonian term through the rotation operator in order to simplify the expression in the next step, where the two complex conjugates should cancel out. The detailed working out is presented below:

$$
\begin{aligned}
U(H/\hbar)U^{\dagger} =&\frac{\tau}{2}\sigma_z + \Big(Icos(\frac{1}{2}\omega t) + i\sigma_z sin(\frac{1}{2}\omega t)\Big)\Big(Icos(\frac{1}{2}\omega t)\frac{\epsilon}{2}\sigma_x - i\frac{\epsilon}{2}sin(\frac{1}{2}\omega t)(\sigma_z\sigma_x - 2i\sigma_y)\Big)\\
=&\frac{\tau}{2}\sigma_z + \Big(\underbrace{Icos(\frac{1}{2}\omega t) + i\sigma_z sin(\frac{1}{2}\omega t)\Big)\Big([Icos(\frac{1}{2}\omega t) - i\sigma_z sin(\frac{1}{2}\omega t)]}_{=e^{i\frac{1}{2}\omega t\sigma_z} * e^{-i\frac{1}{2}\omega t\sigma_z}=1}\frac{\epsilon}{2}\sigma_x - 2\sigma_y\frac{\epsilon}{2}sin(\frac{1}{2}\omega t)\Big)\\
=&\frac{\tau}{2}\sigma_z + \frac{\epsilon}{2}\sigma_x - \frac{\epsilon}{2}2Icos(\frac{1}{2}\omega t)sin(\frac{1}{2}\omega t)\sigma_y - 2i\frac{\epsilon}{2}sin^2(\frac{1}{2}\omega t)\sigma_z\sigma_y =\\
=&\frac{\tau}{2}\sigma_z + \frac{\epsilon}{2}\Big(\sigma_x - 2Icos(\frac{1}{2}\omega t)sin(\frac{1}{2}\omega t)\sigma_y - 2sin^2(\frac{1}{2}\omega t)\sigma_x\Big) =\\
=&\frac{\tau}{2}\sigma_z + \frac{\epsilon}{2}\Big(\underbrace{(1 - 2sin^2(\frac{1}{2}\omega t)}_{=cos(2\frac{1}{2}\omega t)}\sigma_x - \underbrace{2Icos(\frac{1}{2}\omega t)sin(\frac{1}{2}\omega t)}_{=sin(2\frac{1}{2}\omega t)}\sigma_y\Big) =\\
=&\frac{\tau}{2}\sigma_z + \frac{\epsilon}{2}\Big(cos(\omega t)\sigma_x - sin(\omega t)\sigma_y\Big) =\\
=&\frac{\tau}{2}\sigma_z + \frac{\epsilon_0}{2}cos(\omega t)\Big(cos(\omega t)\sigma_x - sin(\omega t)\sigma_y\Big) =\\
=&\frac{\tau}{2}\sigma_z + \frac{\epsilon_0}{2}\Big(cos^2(\omega t)\sigma_x - sin(\omega t)cos(\omega t)\sigma_y + \frac{\sigma_x}{2} - \frac{\sigma_x}{2}\Big) =\\
=&\frac{\tau}{2}\sigma_z + \frac{\epsilon_0}{2}\frac{1}{2}\Big(\underbrace{(2cos^2(\omega t) - 1}_{=cos(2\omega t)})\sigma_x - \underbrace{2sin(\omega t)cos(\omega t)}_{=sin(2\omega t)}\sigma_y + \sigma_x\Big) =\\
=&\frac{\tau}{2}\sigma_z + \frac{\epsilon_0}{4}\Big(\sigma_x + cos(2\omega t)\sigma_x - sin(2\omega t)\sigma_y\Big)
\end{aligned}
$$

The full Hamiltonian in the rotating frame can thus be written as[1]

$$
\begin{aligned}
\tilde{H}/\hbar =&U(H/\hbar)U^{\dagger} + i\dot{U}U^{\dagger} =\\
=&\frac{\tau}{2}\sigma_z + \frac{\epsilon_0}{4}\Big(\sigma_x + cos(2\omega t)\sigma_x - sin(2\omega t)\sigma_y\Big) - \frac{1}{2}\omega\sigma_z\\
=&\frac{\tau - \omega}{2}\sigma_z + \frac{e\alpha V_{rf}}{\hbar}\frac{1}{4}\Big(\sigma_x + cos(2\omega t)\sigma_x - sin(2\omega t)\sigma_y\Big)\\
=&\frac{\Delta}{2}\sigma_z + \frac{\Omega}{4}\Big(\sigma_x + cos(2\omega t)\sigma_x - sin(2\omega t)\sigma_y\Big)
\end{aligned}
\tag{A.6}
$$

with $\Delta = \tau - \omega$ and $\Omega = \frac{e\alpha V_{rf}}{\hbar}$.

A.2 Time-Averaged Population of the Ground State

Further simplifications to A.6 above are limited due to timescales of our system. We cannot neglect the counter-rotating terms at 2ω by making a rotating-wave approximation, as the detuning Δ is often on the orders of GHz. However, as the system is expected to dephase rapidly when excited, and we are not in particular interested in the fast time dynamics, we can assume that all time dependent terms lead to random

---

[1] This equation is in slight deviation with the equation obtained in [66]. In particular, there is a difference of a factor 1/2 for zero phase of the RF field. This difference must come from the fact that our expression for the driving field only includes the cosine term, which adds an additional factor of one half.

phase jumps in the driven frame, rather than coherent precession. The two Hamiltonian of our interest are the time-independent part of A.6 with (H_1) and without (H_2) the presence of the driving field:

$$H_1/\hbar = \frac{1}{2}\begin{pmatrix} \Delta & \Omega_0 \\ \Omega_0 & -\Delta \end{pmatrix} \quad \text{(A.7)} \qquad H_2/\hbar = \frac{1}{2}\begin{pmatrix} \Delta & 0 \\ 0 & -\Delta \end{pmatrix} \quad \text{(A.8)}$$

with $\Delta = \tau - \omega$ and $\Omega_0 = e\alpha V_{rf}/2\hbar$. This allows us to determine the time-averaged population in the ground state p_{gs} simply as the overlap probability of the ground state eigenvector with the original ground state,

$$p_{gs} = |\langle g_1 | g_2 \rangle|^2, \tag{A.9}$$

with g_i the ground state of corresponding Hamiltonian. By obtaining the eigenvalues λ and eigenvectors $\overrightarrow{v}$ through the usual calculation, $det(H - I\lambda) = 0$ and $(H - I\lambda)\overrightarrow{v} = 0$, the ground state eigenvectors and eigenvalues are then

$$\lambda_{1,g} = -\,\hbar\Omega_{eff}/2 \qquad \lambda_{2,g} = -\,\hbar\Delta/2$$

$$v_{1,g} = \begin{pmatrix} -\Omega_0/(\Delta + \Omega_{eff}) \\ 1 \end{pmatrix} \qquad v_{2,g} = \begin{pmatrix} 0 \\ 1 \end{pmatrix}$$

with $\Omega_{eff} = \sqrt{\Delta^2 + \Omega_0^2}$. After normalising, this leads to the final result:

$$p_{gs}^{(1)} = \frac{\Omega_0^2}{\Omega_0^2 + (\Delta - \Omega_{eff})^2}. \tag{A.10}$$

In a slightly more radical approach, we could assume that the state vector jumps randomly between the limiting values of p_{gs}. Then, the time time-averaged ground state probability can be expressed in terms of half the maximum excited state probability from a detuned Rabi oscillation $p_{gs}^{(2)} = 1 - \Omega_0^2/2\Omega_{eff}^2$. For a full tunnel splitting $2t_c = 8\ GHz$ and typical circuit parameters (similar to those reported in ref. [48]), $\alpha \approx 0.75, \Delta \approx 7.5\ GHz$ the relation between the excited state probabilities and the applied RF voltage (translated into readout power in the right panel, assuming quality factor $Q = 250$ and the capacitance of the resonator $C = 0.3\ pF$) is shown in Fig. A.1.

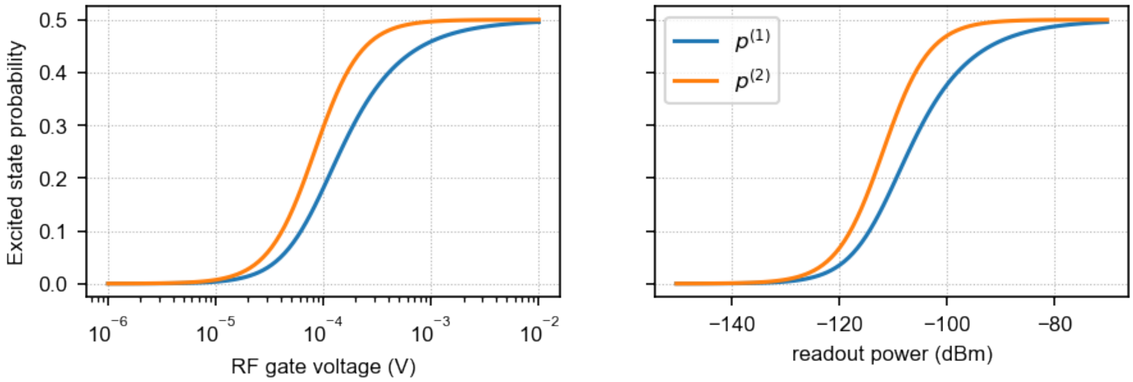

FIGURE A.1: The probability of driving to the excited state as a function of RF voltage (left) and translated into readout power (right).

Appendix B

Tunnelling Between SC and QD

To understand the CSD as one in figure 4.2b, let us visualise the density of state of the system on charge degeneracies. Let us consider decreasing the voltage of the plunger gate of the normal quantum dot while leaving the chemical potential of the superconducting island intact. That corresponds to moving *left* across a horizontal line on the CSD (along the arrow in Fig. B.1), and energy levels of the quantum dot moving *upwards*, with respect to the superconductor. As the superconductivity in our sample occurs via proximity effect, we might expect some subgap states (blue lines within the gap) at $\widetilde{\Delta} < \Delta$ above the Cooper pair condensate (at the dashed line). The relationship between different energy scales of the system is $\widetilde{\Delta} < E_C^{SC}$, making the quasiparticle states accessible, and allowing the even-odd pattern to be observed.

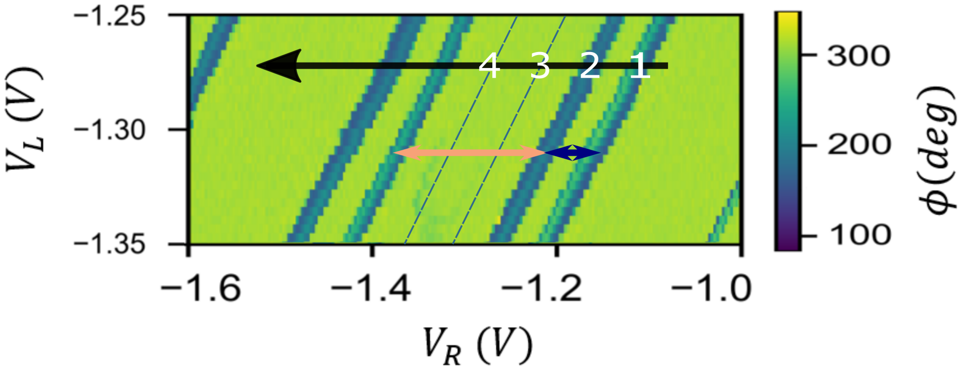

FIGURE B.1: Charge stability diagram; resonator phase shift as a function of the plunger gates on the SC and the normal QD. The orange line indicates the even regime, the blue one, odd regime. The energy spacings in terms of the charging energies superconducting gap are given below. Dotted lines indicate where the empty energy level of the QD is aligned with the energy state of the SC where quasiparticles might be located. Numbers denote different energy configurations of the SC and the QD, schematically shown below. [Comment on whether the voltage on the SC is kept at the value indicated on the plot.]

$$\text{Even regime:} \quad E_C^{SC} + E_C^{QD} + 2\widetilde{\Delta} \tag{B.1}$$

$$\text{Odd regime:} \quad E_C^{SC} + E_C^{QD} - 2\widetilde{\Delta} \tag{B.2}$$

If quasiparticles indeed tunnel from the island, the signal would be visible along the two dashed lines, located $2\widetilde{\Delta}$ from each side within the even regime. The spacing between the two dashed lines, representing two lines of excess quasiparticle transition, is the same as the odd spacing.

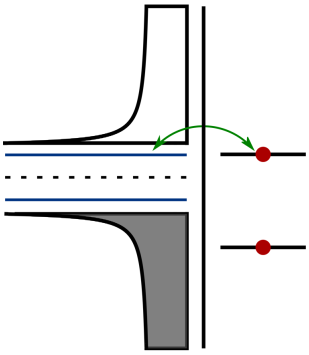

FIGURE B.2: The right of the pair of parallel lines indicates a tunnelling event when the energy level of the quantum dot is aligned (degenerate) with the lowest available single-particle energy state above the gap (number 1 in Fig. B.1). At this point, the energy cost of an electron being on the quantum dot is the same as for the electron on the superconductor, hence the electron is free to tunnel between the two. This can be visible as a shift in the phase (and amplitude) of the reflected RF signal.

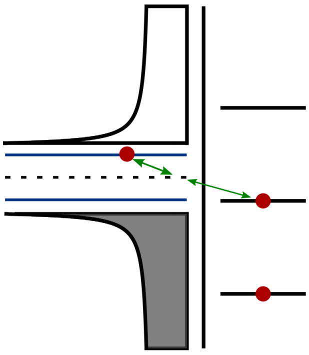

FIGURE B.3: The left of the pair of parallel lines indicates a tunnelling event when the energy level of the quantum dot is aligned (degenerate) with the lowest single-particle energy state below the gap (number 2 in Fig. B.1). At this point, the two electron can recombine into a Cooper pair. An alternative way of seeing this process is an electron tunnelling into the available *hole quasiparticle* below the gap, which became available when the electron from that energy state recombined with an existing electron (quasiparticle) on the island. As before, this results in a shift in the phase (and amplitude) of the reflected RF signal. Notice that compared to the previous situation, the change in energy, and thus the *odd spacing* is given by $E_C^{QD} + E_C^{SC} - 2\widetilde{\Delta}$, accounting for the energy needed for adding an electron to the SC.

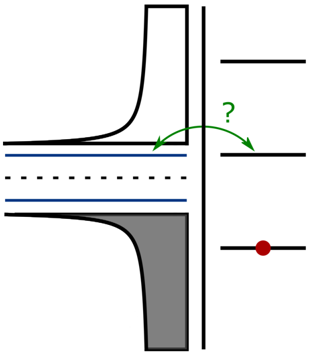

FIGURE B.4: Shifted $2\widetilde{\Delta}$ from the last point, the empty energy level of the quantum dot aligns with the lowest single-particle subgap state on the superconductor (number 3 in Fig. B.1). If quasiparticles are present on the island on the subgap state, they can tunnel between the SC island and the dot, which again should results in a shift in the phase (and amplitude) of the reflected RF signal.

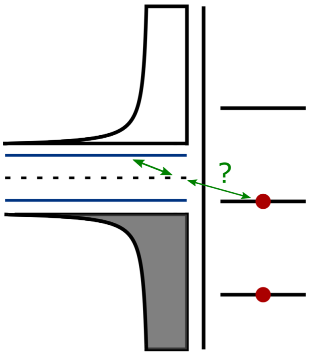

FIGURE B.5: The hole-symmetric process of the one above is depicted here (number 4 in Fig. B.1). In this case, an electron from the quantum dot can recombine with a quasiparticle from the SC. An alternative view of the process is an electron from the sea of electrons below the condensate recombining with the quasiparticle from above the condensate, leaving behind a hole quasiparticle to which an electron from the dot can tunnel. This should again result in a shift in the phase (and amplitude) of the reflected RF signal. After this, the full cycle is completed, and the system is again in the state presented in B.2.

Appendix C

Additional Measurement Figures

C.1 Pinchoff Curves

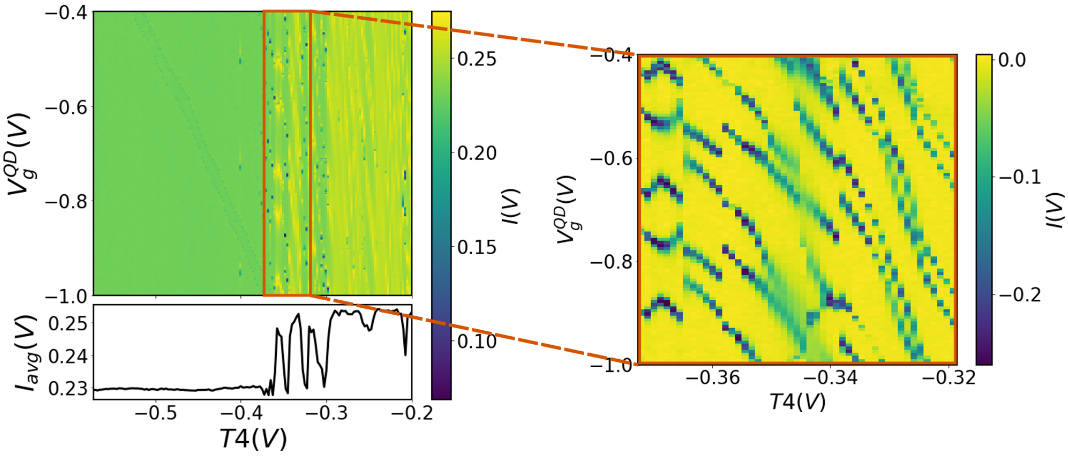

FIGURE C.1: RF Pinchoff curves for the interdot gate T4 for the first sample. By investigating the RF response between the two dots, pinchoff curves for the gate can be plotted, and we can determine what voltage provides weak tunnelling across it. (Upper-left plot) A full map of the I component of the signal, as a function of the gate voltage. An averaged I value is plotted in the left-lower panel. A zoomed-in scan of the same graph is provided in the right panel, clearly showing bright, 2e periodic lines around roughly $T4 = -0.36V$, with a pinched-off regime at values below $\sim -0.4V$.

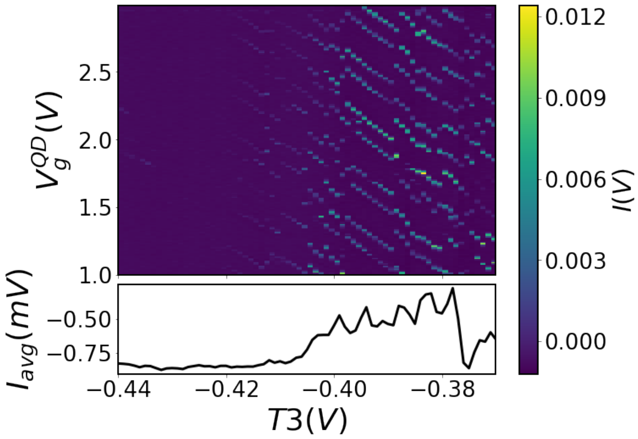

FIGURE C.2: The RF pinchoff curves for the interdot gate T3 for the second sample. (Upper plot) A full map of the I component of the signal, as a function of the gate voltage. An averaged I value is plotted in the lower panel. The gate value of $T4 = -0.4V$ gives a clear and bright 2e spacing.

C.2 Energy Characterisation

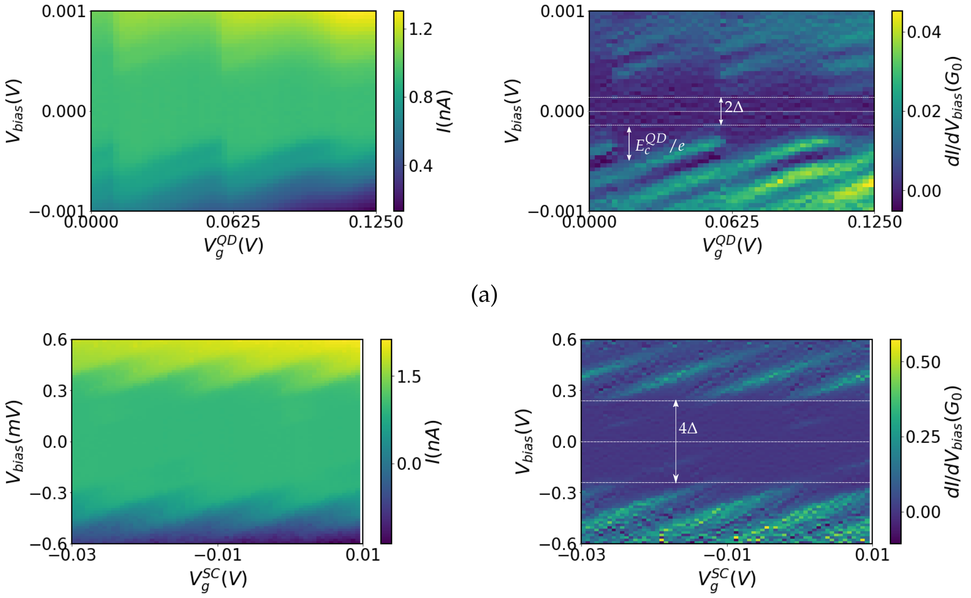

(a)

(b)

FIGURE C.3: Coulomb diamonds of the first device for the normal **(a)** QD and **(b)** SC island. The left panel shows current as a function of gate voltage and bias, while the right figure shows differential conductance (numerical derivative of the current, with respect to the bias voltage) in units of *conductance quantum*. For the SC island, the leads are normal while the dot is superconducting. The two-electron transport cycles produce the the diamonds that are four times higher and twice as wide as in the case of single electron transport.

C.3 Resonator Responses - Determining the resonant frequencies

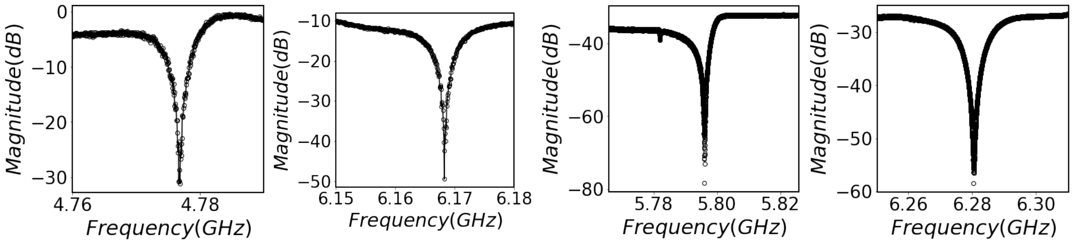

(a)

(b)

(c)

(d)

FIGURE C.4: Resonator response around the resonant frequencies for the two devices. **(a)** QD on the first device ($\omega_0 = 4.77674\ GHz$) **(b)** SC island on the first device ($\omega_0 = 6.16824\ GHz$) **(c)** QD on the second device ($\omega_0 = 5.79548\ GHz$) **(d)** SC island on the second device ($\omega_0 = 6.27949\ GHz$).

C.4 Power Scan

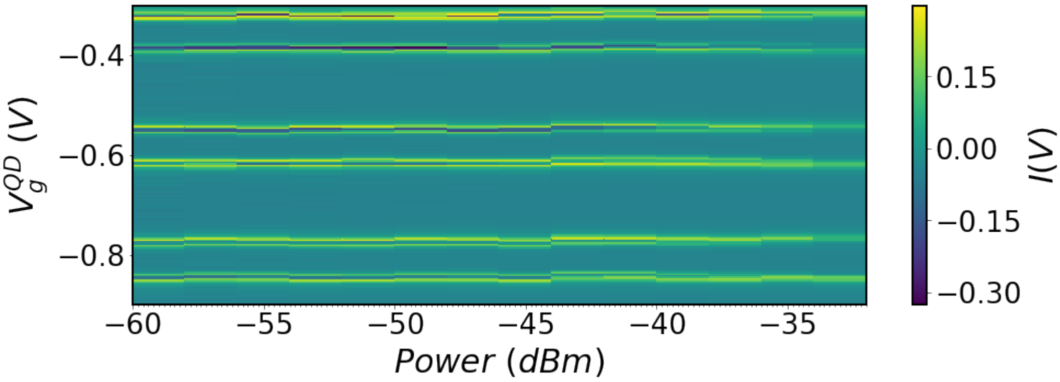

FIGURE C.5: In-phase component versus gate voltage versus applied resonator power, in units of dBm (power ratio with reference to one milliwatt, referenced relative to a 50-ohm impedance. It can be seen from the diagram, that at higher powers the contrast between the signal and background is reduced, possibly due to the destructively interfering quantum capacitances of the excited states driven by large power, relative to the ground state. Another affecting factor is that at around -40 dBm (input power, before $\sim$ 70 dB attenuation), TWPA produces less gain, which could result in a lower signal response.

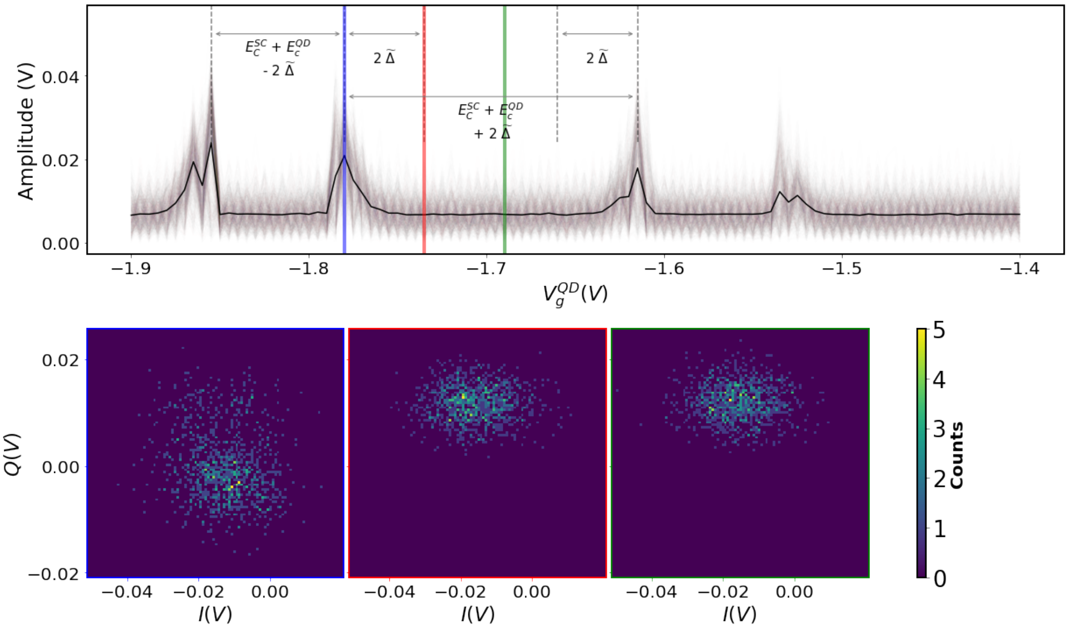

(a)

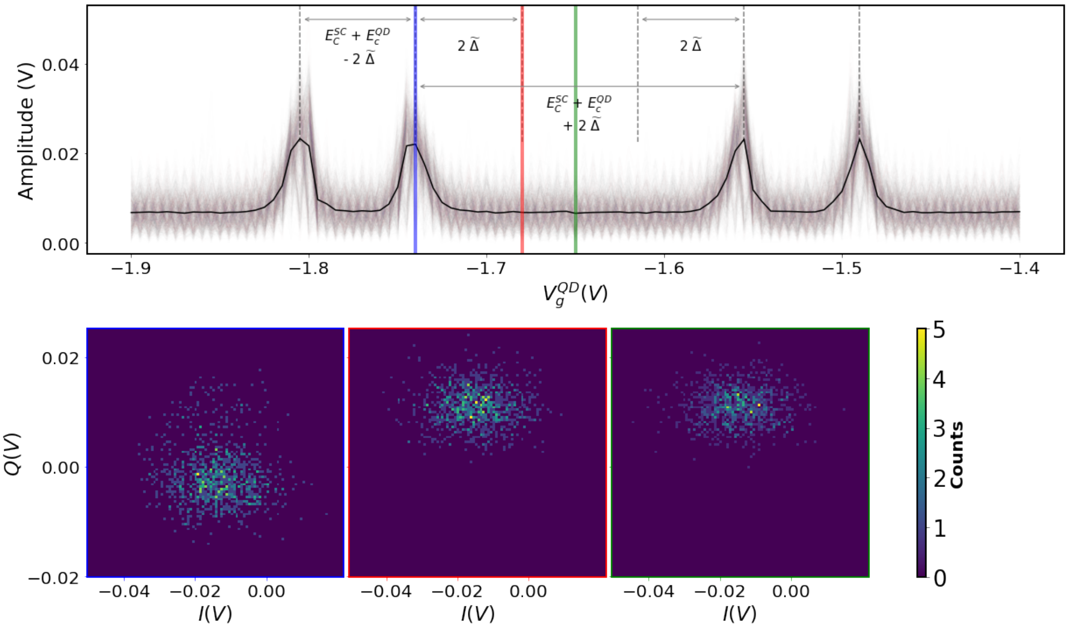

(b)

FIGURE C.6: Power scans as the one in Fig. 4.7, with **(a)** $P = -33\,dBm$ and **(b)** $P = -60\,dBm$.

C.5 Gaussian Division

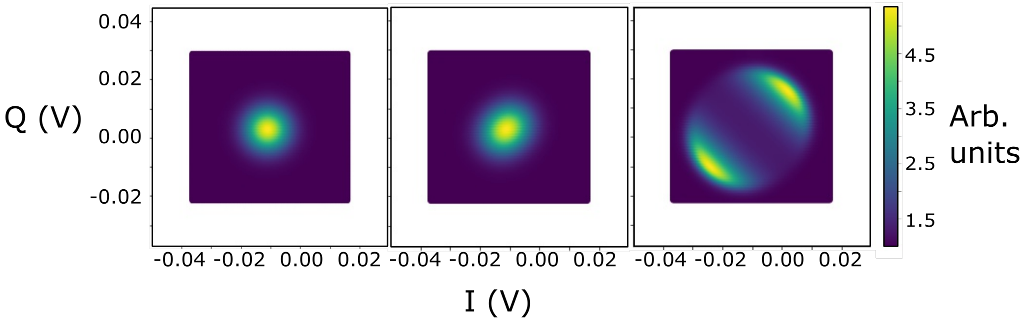

FIGURE C.7: A graphical approach towards splitting observation. Here we illustrate how we can amplify very small splittings or elongations of a distribution. For this, we generated a Gaussian distribution (left figure), and a second one with only a very slight splitting (middle figure), that would be difficult to pick up with a naked eye. If we divide the two spectra, and square the result, we observe a bright corona (right figure), where the original distribution started to split.

Acknowledgements

What a crazy year it has been. From catching 5 am trains from Amsterdam to Delft, to a global pandemic outbreak, causing me to write my thesis from a number of different countries. It is a wonder it has all come together in the end. And there is a large number of people without whom this crazy adventure would have not been possible. I will try to be short and concise, but certainly not because of lack of amazing people that have stood by my side (but rather because I am writing this one hour away from my deadline).

Firstly, thank you Leo and Wolfgang for letting me join your group in the first place. I have felt welcomed and part of the group from day one. I cannot possibly thank you enough for the opportunities you have provided me within the group. Thank you flying me to Copenhagen's labs, thank you for sending me to Veldhoven, and most of all, thank you for inspiring and motivating me every second of the stay. Your energy and the atmosphere you create within the group is something that is often overlooked in importance. I have no doubts that your groups will continue to produce amazing output.

Damaz and Christian, I cannot thank you enough for taking me through this. Many times I have felt lost, and you always knew how to direct me back on the right track. Thank you for being amazing supervisors, your raw brilliance and hard-working mentalities are honestly frightening and inspiring. I have felt supervised as much as I have felt inspired. Thank you for teaching me how important it is to ask questions, and thank you for answering all of the questions I had. I could have not picked better supervisors myself. So thank you for that, and for more, I wish you both nothing but success in future endeavours. Immense gratitude also goes towards the rest of the Cq team. Thank you Jonne for always providing a new fresh perspective on matter at hand, I greatly appreciate your every input that has helped me understand the background physics better. Thank you Filip and Lin for making me feel part of the group, and always providing critical arguments to any discussion. And thank you Michael for accompanying me as a fellow master student in this group. Thank you guys, for providing a great atmosphere and so much opportunity for a scientific discussion. I certainly regret not having more of those with you.

Thank you Peter, for helping with logistics from the UU side. It has certainly made it easier for me, and letting me focus my attention further to quasiparticles.

In nazadnje še hvala mojemu glavnemu emocionalnemu sponzorju skozi zadnjih pet let. Brezopisno vas cenim, in sem vam v dolgovih bolj kot komurkoli. Prav nič od celotne zbirke strani nad tem besedilom ne bi bilo uresničljivo brez vaše konstante podpore, neumajne ljubezni in tisočih spodbud. Hvala, hvala, hvala!

And lastly, I need to thank the person who has encouraged me and supported me (literally) every second over the last few months. Simona, I could not achieve

half of what I achieve if it weren't for you. No words can describe the motivation, confidence and lift you give me daily. Thank you my love.

Bibliography

[1] Peter W. Shor. “Polynomial-Time Algorithms for Prime Factorization and Discrete Logarithms on a Quantum Computer”. In: *SIAM Journal on Computing* 26.5 (1997), pp. 1484–1509. DOI: `10.1137/S0097539795293172`. eprint: `https://doi.org/10.1137/S0097539795293172`. URL: `https://doi.org/10.1137/S0097539795293172`.

[2] Lov K. Grover. “A fast quantum mechanical algorithm for database search”. In: *arXiv e-prints*, quant-ph/9605043 (May 1996), quant–ph/9605043. arXiv: `quant-ph/9605043 [quant-ph]`.

[3] Charles H. Bennett and Gilles Brassard. “Quantum cryptography: Public key distribution and coin tossing”. In: *Theoretical Computer Science* 560 (2014). Theoretical Aspects of Quantum Cryptography – celebrating 30 years of BB84, pp. 7 –11. ISSN: 0304-3975. DOI: `https://doi.org/10.1016/j.tcs.2014.05.025`. URL: `http://www.sciencedirect.com/science/article/pii/S0304397514004241`.

[4] Richard P. Feynman. “Simulating physics with computers”. In: *International Journal of Theoretical Physics* 21.6 (June 1982), pp. 467–488. ISSN: 1572-9575. DOI: `10.1007/BF02650179`. URL: `https://doi.org/10.1007/BF02650179`.

[5] David P. Divincenzo. “The Physical Implementation of Quantum Computation”. In: *Fortschritte der Physik* 48.9-11 (Jan. 2000), pp. 771–783. DOI: `10.1002/1521-3978(200009)48:9/11<771::AID-PROP771>3.0.CO;2-E`. arXiv: `quant-ph/0002077 [quant-ph]`.

[6] Ashley Montanaro. “Quantum algorithms: an overview”. In: *npj Quantum Information* 2.1 (2016), p. 15023. ISSN: 2056-6387. DOI: `10.1038/npjqi.2015.23`. URL: `https://doi.org/10.1038/npjqi.2015.23`.

[7] T. D. Ladd et al. “Quantum computers”. In: *Nature* 464.7285 (Mar. 2010), pp. 45–53. ISSN: 1476-4687. DOI: `10.1038/nature08812`. URL: `https://doi.org/10.1038/nature08812`.

[8] Michael A. Nielsen and Isaac L. Chuang. *Quantum Computation and Quantum Information: 10th Anniversary Edition*. 10th. USA: Cambridge University Press, 2011. ISBN: 1107002176.

[9] Earl T. Campbell, Barbara M. Terhal, and Christophe Vuillot. “Roads towards fault-tolerant universal quantum computation”. In: *Nature* 549.7671 (Sept. 2017), pp. 172–179. DOI: `10.1038/nature23460`. arXiv: `1612.07330 [quant-ph]`.

[10] David Aasen et al. "Milestones Toward Majorana-Based Quantum Computing". In: *Physical Review X* 6.3, 031016 (July 2016), p. 031016. DOI: `10.1103/PhysRevX.6.031016`. arXiv: `1511.05153 [cond-mat.mes-hall]`.

[11] Chetan Nayak et al. "Non-Abelian anyons and topological quantum computation". In: *Reviews of Modern Physics* 80.3 (July 2008), pp. 1083–1159. DOI: `10.1103/RevModPhys.80.1083`. arXiv: `0707.1889 [cond-mat.str-el]`.

[12] Parsa Bonderson, Michael Freedman, and Chetan Nayak. "Measurement-Only Topological Quantum Computation". In: *Phys. Rev. Lett.* 101 (1 2008), p. 010501. DOI: `10.1103/PhysRevLett.101.010501`. URL: `https://link.aps.org/doi/10.1103/PhysRevLett.101.010501`.

[13] Torsten Karzig et al. "Scalable designs for quasiparticle-poisoning-protected topological quantum computation with Majorana zero modes". In: *Phys. Rev. B* 95 (23 2017), p. 235305. DOI: `10.1103/PhysRevB.95.235305`. URL: `https://link.aps.org/doi/10.1103/PhysRevB.95.235305`.

[14] Stephan Plugge et al. "Majorana box qubits". In: *New Journal of Physics* 19.1 (2017), p. 012001. DOI: `10.1088/1367-2630/aa54e1`. URL: `https://doi.org/10.1088%2F1367-2630%2Faa54e1`.

[15] A. Yu Kitaev. "6. QUANTUM COMPUTING: Unpaired Majorana fermions in quantum wires". In: *Physics Uspekhi* 44.10S (Oct. 2001), p. 131. DOI: `10.1070/1063-7869/44/10S/S29`. arXiv: `cond-mat/0010440 [cond-mat.mes-hall]`.

[16] Liang Fu and C. L. Kane. "Superconducting Proximity Effect and Majorana Fermions at the Surface of a Topological Insulator". In: *Phys. Rev. Lett.* 100 (9 2008), p. 096407. DOI: `10.1103/PhysRevLett.100.096407`. URL: `https://link.aps.org/doi/10.1103/PhysRevLett.100.096407`.

[17] Christina Knapp et al. "Dephasing of Majorana-based qubits". In: *Phys. Rev. B* 97 (12 2018), p. 125404. DOI: `10.1103/PhysRevB.97.125404`. URL: `https://link.aps.org/doi/10.1103/PhysRevB.97.125404`.

[18] Torsten Karzig, William S. Cole, and Dmitry I. Pikulin. "Quasiparticle poisoning of Majorana qubits". In: *arXiv e-prints*, arXiv:2004.01264 (Apr. 2020), arXiv:2004.01264. arXiv: `2004.01264 [cond-mat.mes-hall]`.

[19] John M. Martinis, M. Ansmann, and J. Aumentado. "Energy Decay in Superconducting Josephson-Junction Qubits from Nonequilibrium Quasiparticle Excitations". In: *Phys. Rev. Lett.* 103 (9 2009), p. 097002. DOI: `10.1103/PhysRevLett.103.097002`. URL: `https://link.aps.org/doi/10.1103/PhysRevLett.103.097002`.

[20] A. J. Ferguson et al. "Microsecond Resolution of Quasiparticle Tunneling in the Single-Cooper-Pair Transistor". In: *Phys. Rev. Lett.* 97 (10 2006), p. 106603. DOI: `10.1103/PhysRevLett.97.106603`. URL: `https://link.aps.org/doi/10.1103/PhysRevLett.97.106603`.

[21] D. Ristè et al. "Millisecond charge-parity fluctuations and induced decoherence in a superconducting transmon qubit". In: *Nature Communications* 4.1 (2013), p. 1913. ISSN: 2041-1723. DOI: 10.1038/ncomms2936. URL: https://doi.org/10.1038/ncomms2936.

[22] V. F. Maisi et al. "Excitation of Single Quasiparticles in a Small Superconducting Al Island Connected to Normal-Metal Leads by Tunnel Junctions". In: *Phys. Rev. Lett.* 111 (14 2013), p. 147001. DOI: 10.1103/PhysRevLett.111.147001. URL: https://link.aps.org/doi/10.1103/PhysRevLett.111.147001.

[23] Diego Rainis and Daniel Loss. "Majorana qubit decoherence by quasiparticle poisoning". In: *Phys. Rev. B* 85 (17 2012), p. 174533. DOI: 10.1103/PhysRevB.85.174533. URL: https://link.aps.org/doi/10.1103/PhysRevB.85.174533.

[24] S. M. Albrecht et al. "Transport Signatures of Quasiparticle Poisoning in a Majorana Island". In: *Phys. Rev. Lett.* 118 (13 2017), p. 137701. DOI: 10.1103/PhysRevLett.118.137701. URL: https://link.aps.org/doi/10.1103/PhysRevLett.118.137701.

[25] A. P. Higginbotham et al. "Parity lifetime of bound states in a proximitized semiconductor nanowire". In: *Nature Physics* 11.12 (2015), pp. 1017–1021. ISSN: 1745-2481. DOI: 10.1038/nphys3461. URL: https://doi.org/10.1038/nphys3461.

[26] Gerbold C. Ménard et al. "Suppressing quasiparticle poisoning with a voltage-controlled filter". In: *Phys. Rev. B* 100 (16 2019), p. 165307. DOI: 10.1103/PhysRevB.100.165307. URL: https://link.aps.org/doi/10.1103/PhysRevB.100.165307.

[27] Michael Tinkham. *Introduction to Superconductivity*. 2nd ed. Dover Publications, June 2004. ISBN: 0486435032. URL: http://www.worldcat.org/isbn/0486435032.

[28] Anton Bespalov et al. "Theoretical Model to Explain Excess of Quasiparticles in Superconductors". In: *Phys. Rev. Lett.* 117 (11 2016), p. 117002. DOI: 10.1103/PhysRevLett.117.117002. URL: https://link.aps.org/doi/10.1103/PhysRevLett.117.117002.

[29] Alexandre Blais et al. "Cavity quantum electrodynamics for superconducting electrical circuits: An architecture for quantum computation". In: *Phys. Rev. A* 69 (6 2004), p. 062320. DOI: 10.1103/PhysRevA.69.062320. URL: https://link.aps.org/doi/10.1103/PhysRevA.69.062320.

[30] Leo P Kouwenhoven et al. "Electron transport in quantum dots". In: *Mesoscopic electron transport*. Springer, 1997, pp. 105–214.

[31] R. Hanson et al. "Spins in few-electron quantum dots". In: *Rev. Mod. Phys.* 79 (4 2007), pp. 1217–1265. DOI: 10.1103/RevModPhys.79.1217. URL: https://link.aps.org/doi/10.1103/RevModPhys.79.1217.

[32] L. P. Kouwenhoven et al. "Single electron charging effects in semiconductor quantum dots". In: *Zeitschrift für Physik B Condensed Matter* 85.3 (1991), pp. 367–373. ISSN: 1431-584X. DOI: `10.1007/BF01307632`. URL: `https://doi.org/10.1007/BF01307632`.

[33] Wilfred G Van der Wiel et al. "Electron transport through double quantum dots". In: *Reviews of Modern Physics* 75.1 (2002), p. 1.

[34] H Kamerlingh Onnes. "The resistance of pure mercury at helium temperatures". In: *Commun. Phys. Lab. Univ. Leiden, b* 120 (1911).

[35] W. Meissner and R. Ochsenfeld. "Ein neuer Effekt bei Eintritt der Supraleitfähigkeit". In: *Naturwissenschaften* 21.44 (1933), pp. 787–788. ISSN: 1432-1904. DOI: `10.1007/BF01504252`. URL: `https://doi.org/10.1007/BF01504252`.

[36] J. Bardeen, L. N. Cooper, and J. R. Schrieffer. "Theory of Superconductivity". In: *Phys. Rev.* 108 (5 1957), pp. 1175–1204. DOI: `10.1103/PhysRev.108.1175`. URL: `https://link.aps.org/doi/10.1103/PhysRev.108.1175`.

[37] N. N. Bogoljubov. "On a new method in the theory of superconductivity". In: *Il Nuovo Cimento (1955-1965)* 7.6 (1958), pp. 794–805. ISSN: 1827-6121. DOI: `10.1007/BF02745585`. URL: `https://doi.org/10.1007/BF02745585`.

[38] L. DiCarlo et al. "Differential Charge Sensing and Charge Delocalization in a Tunable Double Quantum Dot". In: *Phys. Rev. Lett.* 92 (22 2004), p. 226801. DOI: `10.1103/PhysRevLett.92.226801`. URL: `https://link.aps.org/doi/10.1103/PhysRevLett.92.226801`.

[39] R. J. Schoelkopf et al. "The Radio-Frequency Single-Electron Transistor (RF-SET): A Fast and Ultrasensitive Electrometer". In: *Science* 280.5367 (1998), pp. 1238–1242. ISSN: 0036-8075. DOI: `10.1126/science.280.5367.1238`. eprint: `https://science.sciencemag.org/content/280/5367/1238.full.pdf`. URL: `https://science.sciencemag.org/content/280/5367/1238`.

[40] S. Probst et al. "Efficient and robust analysis of complex scattering data under noise in microwave resonators". In: *Review of Scientific Instruments* 86.2 (2015), p. 024706. DOI: `10.1063/1.4907935`. eprint: `https://doi.org/10.1063/1.4907935`. URL: `https://doi.org/10.1063/1.4907935`.

[41] David M Pozar. *Microwave engineering; 3rd ed.* Hoboken, NJ: Wiley, 2005. URL: `https://cds.cern.ch/record/882338`.

[42] R. Mizuta et al. "Quantum and tunneling capacitance in charge and spin qubits". In: *Phys. Rev. B* 95 (4 2017), p. 045414. DOI: `10.1103/PhysRevB.95.045414`. URL: `https://link.aps.org/doi/10.1103/PhysRevB.95.045414`.

[43] T. Duty et al. "Observation of Quantum Capacitance in the Cooper-Pair Transistor". In: *Phys. Rev. Lett.* 95 (20 2005), p. 206807. DOI: `10.1103/PhysRevLett.95.206807`. URL: `https://link.aps.org/doi/10.1103/PhysRevLett.95.206807`.

[44] M. D. Schroer et al. “Radio Frequency Charge Parity Meter”. In: *Phys. Rev. Lett.* 109 (16 2012), p. 166804. DOI: 10.1103/PhysRevLett.109.166804. URL: https://link.aps.org/doi/10.1103/PhysRevLett.109.166804.

[45] K. D. Petersson et al. “Charge and Spin State Readout of a Double Quantum Dot Coupled to a Resonator”. In: *Nano Letters* 10.8 (2010), pp. 2789–2793. ISSN: 1530-6984. DOI: 10.1021/nl100663w. URL: https://doi.org/10.1021/nl100663w.

[46] M. Esterli, R. M. Otxoa, and M. F. Gonzalez-Zalba. “Small-signal equivalent circuit for double quantum dots at low-frequencies”. In: *Applied Physics Letters* 114.25 (2019), p. 253505. DOI: 10.1063/1.5098889. eprint: https://doi.org/10.1063/1.5098889. URL: https://doi.org/10.1063/1.5098889.

[47] Matias Urdampilleta et al. “Charge Dynamics and Spin Blockade in a Hybrid Double Quantum Dot in Silicon”. In: *Phys. Rev. X* 5 (3 2015), p. 031024. DOI: 10.1103/PhysRevX.5.031024. URL: https://link.aps.org/doi/10.1103/PhysRevX.5.031024.

[48] Damaz de Jong et al. “Rapid Detection of Coherent Tunneling in an In As Nanowire Quantum Dot through Dispersive Gate Sensing”. In: *Physical Review Applied* 11.4, 044061 (Apr. 2019), p. 044061. DOI: 10.1103/PhysRevApplied.11.044061. arXiv: 1812.08609 [cond-mat.mes-hall].

[49] K. D. Petersson et al. “Circuit quantum electrodynamics with a spin qubit”. In: *Nature* 490.7420 (2012), pp. 380–383. ISSN: 1476-4687. DOI: 10.1038/nature11559. URL: https://doi.org/10.1038/nature11559.

[50] Gustav Teleberg and Graham Batey. “Principles of dilution refrigeration.” In: *Oxford Instruments Nanoscience* (2015).

[51] Frank Pobell. “The 3 He–4 He Dilution Refrigerator”. In: *Matter and Methods at Low Temperatures*. Springer, 2007, pp. 149–189.

[52] Ananda Roy and Michel Devoret. “Introduction to parametric amplification of quantum signals with Josephson circuits”. In: *Comptes Rendus Physique* 17.7 (2016). Quantum microwaves / Micro-ondes quantiques, pp. 740 –755. ISSN: 1631-0705. DOI: https://doi.org/10.1016/j.crhy.2016.07.012. URL: http://www.sciencedirect.com/science/article/pii/S1631070516300640.

[53] Daan Waardenburg. “On-chip circuit design for capacitive gate based readout.” MA thesis. the Netherlands: Delft University of Technology, 2019.

[54] M. Göppl et al. “Coplanar waveguide resonators for circuit quantum electrodynamics”. In: *Journal of Applied Physics* 104.11 (2008), p. 113904. DOI: 10.1063/1.3010859. eprint: https://doi.org/10.1063/1.3010859. URL: https://doi.org/10.1063/1.3010859.

[55] M. T. Tuominen et al. “Experimental evidence for parity-based 2e periodicity in a superconducting single-electron tunneling transistor”. In: *Phys. Rev. Lett.* 69 (13 1992), pp. 1997–2000. DOI: 10.1103/PhysRevLett.69.1997. URL: https://link.aps.org/doi/10.1103/PhysRevLett.69.1997.

[56] J. Aumentado et al. “Nonequilibrium Quasiparticles and 2*e* Periodicity in Single-Cooper-Pair Transistors”. In: *Phys. Rev. Lett.* 92 (6 2004), p. 066802. DOI: 10.1103/PhysRevLett.92.066802. URL: https://link.aps.org/doi/10.1103/PhysRevLett.92.066802.

[57] O. Naaman and J. Aumentado. “Time-domain measurements of quasiparticle tunneling rates in a single-Cooper-pair transistor”. In: *Phys. Rev. B* 73 (17 2006), p. 172504. DOI: 10.1103/PhysRevB.73.172504. URL: https://link.aps.org/doi/10.1103/PhysRevB.73.172504.

[58] P. J. de Visser et al. “Number Fluctuations of Sparse Quasiparticles in a Superconductor”. In: *Phys. Rev. Lett.* 106 (16 2011), p. 167004. DOI: 10.1103/PhysRevLett.106.167004. URL: https://link.aps.org/doi/10.1103/PhysRevLett.106.167004.

[59] N. A. Court et al. “Quantitative study of quasiparticle traps using the single-Cooper-pair transistor”. In: *Phys. Rev. B* 77 (10 2008), p. 100501. DOI: 10.1103/PhysRevB.77.100501. URL: https://link.aps.org/doi/10.1103/PhysRevB.77.100501.

[60] M. D. Shaw et al. “Kinetics of nonequilibrium quasiparticle tunneling in superconducting charge qubits”. In: *Phys. Rev. B* 78 (2 2008), p. 024503. DOI: 10.1103/PhysRevB.78.024503. URL: https://link.aps.org/doi/10.1103/PhysRevB.78.024503.

[61] J. M. Hergenrother, M. T. Tuominen, and M. Tinkham. “Charge transport by Andreev reflection through a mesoscopic superconducting island”. In: *Phys. Rev. Lett.* 72 (11 1994), pp. 1742–1745. DOI: 10.1103/PhysRevLett.72.1742. URL: https://link.aps.org/doi/10.1103/PhysRevLett.72.1742.

[62] Jasper van Veen et al. “Revealing charge-tunneling processes between a quantum dot and a superconducting island through gate sensing”. In: *Phys. Rev. B* 100 (17 2019), p. 174508. DOI: 10.1103/PhysRevB.100.174508. URL: https://link.aps.org/doi/10.1103/PhysRevB.100.174508.

[63] John F. Cochran and D. E. Mapother. “Superconducting Transition in Aluminum”. In: *Phys. Rev.* 111 (1 1958), pp. 132–142. DOI: 10.1103/PhysRev.111.132. URL: https://link.aps.org/doi/10.1103/PhysRev.111.132.

[64] C. M. Wilson, L. Frunzio, and D. E. Prober. “Time-Resolved Measurements of Thermodynamic Fluctuations of the Particle Number in a Nondegenerate Fermi Gas”. In: *Phys. Rev. Lett.* 87 (6 2001), p. 067004. DOI: 10.1103/PhysRevLett.87.067004. URL: https://link.aps.org/doi/10.1103/PhysRevLett.87.067004.

[65] CM Wilson and DE Prober. “Quasiparticle number fluctuations in superconductors”. In: *Physical Review B* 69.9 (2004), p. 094524.

[66] L. M. K. Vandersypen and I. L. Chuang. “NMR techniques for quantum control and computation”. In: *Rev. Mod. Phys.* 76 (4 2005), pp. 1037–1069. DOI: `10.1103/RevModPhys.76.1037`. URL: `https://link.aps.org/doi/10.1103/RevModPhys.76.1037`.